2013-09-26

Size-based Separation of Bioparticles Using Planar Nanofluidic Devices

Jie Xuan
Brigham Young University - Provo

Size-Based Separation of Bioparticles Using Planar Nanofluidic Devices

Jie Xuan

A dissertation submitted to the faculty of
Brigham Young University
in partial fulfillment of the requirements for the degree of

Doctor of Philosophy

Milton L. Lee, Chair
Adam T. Woolley
Aaron R. Hawkins
Steven W. Graves
Matthew R. Linford

Department of Chemistry and Biochemistry

Brigham Young University

Septermber 2013

ABSTRACT

Size-Based Separation of Bioparticles Using
Planar Nanofluidic Devices

Jie Xuan
Department of Chemistry and Biochemistry, BYU
Doctor of Philosophy

Nanofluidic devices are structures having at least one dimension in the submicron range, which is of the same order of magnitude as the sizes of biomolecules and bioparticles such as proteins and viruses. As a result, size-selective separations are important applications for nanofluidics. Well-defined micro or nano device structures fabricated via micromachining have greatly reduced sample consumption and enabled separations in a parallel fashion, promising significant speed and resolution advantages over conventional size separation techniques, such as gel electrophoresis and size exclusion chromatography. In collaboration with others, I have developed a size separation method using nanofluidic devices consisting of an array of parallel planar nanochannels with varying heights. Separation of nanoparticles is accomplished by simply flowing a liquid suspension of the particles through the nanochannels via capillary action. When a mixture of particles arrives at an interface, where the channel steps from a deeper to a shallower segment, larger particles become trapped and smaller particles pass through, thereby achieving separation. In this dissertation, I demonstrated the successful trapping of polymer nanobeads and two types of virus capsids (30 nm hepatitis B virus capsids and 120 nm herpes simplex virus type 1 capsids) using nanochannels with two different channel height segments. Furthermore, I studied the fractionation of nanoparticles in nanochannels with three different channel height segments. The effects of surfactants and an alternating current electric field on particle distribution were investigated, both of which aided in the prevention of channel clogging. Most recently, I applied the nanosieving method for separating lipoproteins, which are important in the diagnosis of cardiovascular disease. Promising results were obtained, indicating that the major lipoprotein classes, including intermediate density lipoproteins (IDL, 23-35 nm), low-density-lipoproteins (LDL, 18-25 nm) and high-density-lipoproteins (HDL, 5-12 nm), may eventually be fractionated using three-segment nanochannels. To successfully fractionate lipoprotein mixtures, characterization of flow dynamics in three-segment nanochannels, passivation of the surface to prevent nonspecific protein adsorption, application of an electric field to help particles overcome an energy barrier, and use of multi-color fluorescent labeling to assist detection are required. I studied the channel passivation performance of polyethylene glycol (PEG) and used dual-color fluorescence detection for the separation of a binary protein mixture. Finally, I fabricated channels with monotonically changing barrier heights and demonstrated differential trapping of polymer beads. The data trend followed a slit model derived from a model developed by Giddings for size exclusion chromatography.

Keywords: nanosieves, fabrication, trapping, separation, nanoparticles

ACKNOWLEDGEMENTS

Looking back at the end of this journey, I realize there are so many people I need to thank that I don't even know where to start. I would not have been able to make it this far if it were not for their love, help and support. First of all, I would like to express my sincerest gratitude to my mentor, Dr. Milton L. Lee. I am thankful for the example he set for me, for the important things he has taught me in doing research. His guidance and encouragement have helped me through many challenging times. I am most thankful for the fact that he has always believed in me and asked me to keep trying and never give up. I would also like to acknowledge my committee members: Dr. Adam T. Woolley, Dr. Aaron R. Hawkins, Dr. Steven W. Graves and Dr. Matthew R. Linford. I am grateful for the valuable insights they shared with me in their fields. I appreciate greatly their patience and their willingness to help during my studies at BYU.

I want to thank my lab partners, Mark N. Hamblin, John Stout, Meagan Miller, and Suresh Kumar, and cleanroom manager, Jim Fraser, who led me into the world of microfabrication. I am grateful for my colleagues and former graduates from Dr. Lee's and Dr. Woolley's labs: Dan Li, Kun Liu, Pankaj Aggarwal, Sonika Sharma, Xiaofeng Xie, Anzi Wang, Yuanyuan Li, Yun Li, Xuefei Sun, Yansheng Liu, Xin Chen, Yan Fang, Miao Wang, Tai Truong, Jacki Murray, Jesse Contreras, Weichun Yang, Ming Yu, Pamela Nge, Chad Rogers, Debolina Chatterjee and Jayson Pagaduan. I am grateful for the help I received from the faculty and former graduate students in the Biochemistry area: Dr. David M Belnap, Dr. Greg F. Burton, Xueyuan Zhou and Changna Wang. I would also like to thank Dr. John Gardner, Michael Standing and Dr. Jeffrey Farrer for their help with electron microscopy. It has been truly my pleasure working and interacting with these amazing people. Wherever I am in life, I will always remember their friendship.

Last but not least, I want to thank my dear friends and family, who have my back and are always there to lend a helping hand. Their love and friendship make me strong. I would like to dedicate this dissertation to my parents. Their unconditional love has made everything possible.

Table of Contents

List of Figures

List of Tables

Chapter 1. Introduction

1.1 Size separation of biomolecules and bioparticles using micro/nanofabricated structures

A wide range of techniques are traditionally used as size characterization tools, which all have their limitations. Using dynamic light scattering (DLS),[1] accurate measurements become extremely difficult for samples containing a broad particle size distribution, large aggregates, or contaminants. Conventional electron microscopy techniques, such as transmission electron microscopy (TEM),[2] allow the direct visualization of nanoparticles, including their sizes, shapes and degrees of aggregation. However, TEM must be operated under vacuum conditions. Also, sample preparation for TEM is time-consuming, and usually leads to sample alteration during drying. Size separation techniques based on chromatography and field flow fractionation (FFF) provide good resolution and are sensitive and non-destructive. However, size exclusion chromatography (SEC)[3,4] is limited by possible sample loss caused by nonspecific sample-column interactions and limited size separation range, depending on the pore size distribution of the SEC column. Hydrodynamic chromatography (HDC) overcomes most nonspecific interactions by using nonporous beads for column packing. It also allows a wider size separation range from 5 to 1200 nm.[5] However, similar to DLS, HDC suffers from poor resolution. FFF separates macromolecules and particles based on interaction between analytes and a particular applied field. FFF can be used to fractionate particles ranging from 1 nm to 1 μm. However, FFF utilizes complex instrumentation and requires a skilled operator to obtain reproducible and reliable data.[6,7]

For purification and separation, polymer gels and membranes with various pore sizes have been extensively used as molecular sieve matrices. Unfortunately, the microscopic

structures of these systems are inherently random, which hinders both theoretical and experimental studies aimed at improving separations. Microfluidic systems for biomolecule size separation have generally adopted the same random nanoporous sieving materials[8-10] and, hence, the same limitations.

In contrast, carefully designed regular micro/nanostructures via micro/nanofabrication provide unique capability in biomolecule analysis by improving control over the molecular sieving process. The traditional high-performance techniques of liquid chromatography (LC) and capillary electrophoresis (CE) are being miniaturized for efficient, high speed separations.[11] Advantages of miniaturization are low reagent consumption and fast analysis. As separation technologies move from microfluidics to nanofluidics, device dimensions begin to have a significant influence on the behavior of the system.[12,13] By definition, nanofluidics rely on structures that have at least one dimension between 1 nm and 100 nm, which is of the same order of magnitude as the sizes of biomacromolecules such as DNA and proteins. Consequently, size separation becomes a suitable application for nanofluidics. As the channel dimensions approach the particle size, unique phenomena and separation mechanisms are being discovered. For example, due to the large surface-to-volume ratio, it has been shown that fluid transport in nanochannels is different from common understanding at the macroscale.[14-17] Well-defined micro/nanostructures can be precisely designed and fabricated with sub-10 nm resolution.[18-21] Downscaling of device dimensions not only enhances the realization of the "lab-on-a-chip" concept, where sample injection, analysis, detection and signal processing are integrated onto a single chip,[22-25] but more importantly, the deterministic networks of micro/nanostructures provide insights into separation processes, such that better speed and resolution can be achieved.

In the early 1990s, the group of Austin[26] pioneered the use of microfabricated post arrays (0.15 μm-high posts, 1 μm diameter and 2 μm center-to-center spacing) to replace the gel matrix for DNA analysis. Since then, a variety of micro/nanofluidic structures have been developed that utilize different separation mechanisms. The goals of this chapter are to summarize these designs (described here in three categories according to architecture, i.e., micro/nanopillar array structures, nanoplane gap structures and artificial nanoporous membranes), and to discuss their separation mechanisms and applications.

1.2 Micro/nanofabricated pillar array structures

1.2.1 Miniaturized DNA electrophoresis

DNA conformational and electrophoretic behavior. DNA fragments are considered randomly coiled polymers with radius of gyration given by

$$R_g = (bL/6)^{1/2} \quad (1.1)$$

where b = 100 nm is the Kuhn length and L is the contour length (L = number of base pairs × 0.34 nm).[27] When a long DNA molecule is driven into a gel, the DNA chain can hook around the gel fibers, forming a U-shape in the direction of the electric field, and then relax into a more compact state.[28,29] This periodic conformational change was observed in both macroscopic agarose gel electrophoresis and nanopillar arrays.

Agarose gel electrophoresis is one the most common techniques used to determine the size of DNA. It is essentially a sieving process in which DNA molecules migrate through a cross-linked network by an electrophoretic force. Both the size and conformation of the DNA affect how fast it moves inside the gel. Under a uniform electric field, small molecules migrate more quickly than larger ones at rates that are proportional to their sizes. This linear relationship

between size and migration rate is only accurate for DNA molecules smaller than 40 kbp.[30] For longer DNA, the efficiency of agarose gel electrophoresis decreases substantially due to irreversible trapping of DNA in the gel fibers.[31] In 1984, Schwartz and Cantor[32] introduced the method of macroscopic pulsed-field gel electrophoresis (PFGE), which was used for separating long DNA. However, PFGE takes hours to days to separate long DNA. The fractionation process is ill-understood due to the inhomogeneous gel structure. To address the challenging problem of separating long DNA and to better understand the sieving mechanism, miniaturized systems were developed with the hope to eventually replace their macroscopic counterparts.

Depending on the relationship between average pore size (a) and radius of gyration (R_g) of DNA molecules, DNA electrophoretic behavior can be classified into three regimes: Ogston sieving, entropic trapping and reptation. When $a > R_g$, DNA molecules are fractionated by Ogston sieving. Their mobilities can be described by the Ogston-Morris-Rodbard-Chrambach model.[33-35] When $a \approx R_g$, the separation regime is entropic trapping because DNA molecules can freely coil into large pores, whereas there is an entropic cost for them to enter smaller pores. When $a < R_g$, the DNA molecules migrate by "reptation" i.e., a reptile-like, snaking action through the pores.

Pulsed-field gel electrophoresis. The first miniaturization of PFGE for separating DNA was conducted in a two-dimensional array of circular micropillars, [36] taking advantage of a switchback mechanism first suggested by Southern *et al.*[37] In strong fields ($E \sim 10$ V/cm), DNA molecules are stretched into a linear form when the fields are aligned along one of the axes of the array. Different results were observed when acute and obtuse angles between the fields were used. When pulsing using acute angles, all molecules zigzagged through the array at approximately the same speed, and no fractionation was observed. However, when the fields

alternated through obtuse angles, molecules backtracked along the previous path led by their tail ends. Since longer molecules retraced longer paths than shorter ones, fractionation according to molecular weight took place (**Fig. 1.1**). The authors investigated an angle of 120 degrees, so the design was referred to as a hexagonal array. Using this geometry, λ DNA (48.5 kbp) and T4 DNA (165.6 kbp) were separated in ~ 10 s, several orders of magnitude faster than by using conventional techniques.[38] It is worth mentioning that, to eliminate entanglement of large DNA around the posts, the device adopted entropic trapping[39] in low dc fields for sample injection, which helped collect and launch the molecules in a narrow zone and reduced zone broadening.

In another study combining entropic trapping and a pulsed-electric field, DNA molecules were inserted into a densely packed (80 nm diameter, 135 nm spacing) nanopillar array (an entropically unfavorable region) and separated according to size by the fact that shorter molecules moved fully inside the region, while longer molecules straddled across the interface.[40] When the field was switched off, the longer molecules were observed to recoil entirely out of the array to increase their configurational entropy while shorter molecules remained within the pillar array, thereby becoming separated. The same nanostructure used in the entropic recoil separation was first used for DNA mobility characterization in a constant field.[41]

Pulsed-field electrophoresis of DNA in a hexagonal array can be tuned via three factors: pulse duration (frequency), field strength and post size. In the previous examples, the pulse times and field strengths remained the same throughout one separation. As a result, all molecules moved in the direction as defined by the net electric field. If asymmetric fields of varying frequency were used, DNA molecules could be sorted in different directions according to size, resembling the separation of white light in a prism. Therefore, such a device was named a DNA prism. The prism (2 μm diameter, 2 μm spacing and 2 μm tall) separated 61-209 kbp DNA

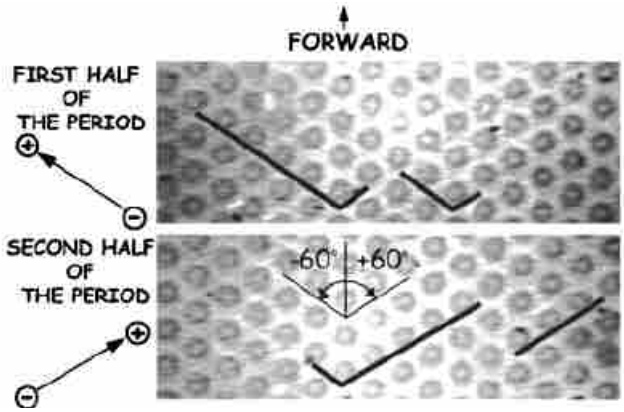

Figure 1.1 Pulsed-field electrophoresis of different-size DNA in a hexagonal array. The fields were alternated along the channels formed at 120˚ by the posts in the array. Longer molecules spent most time retracing the path and, as a result, did not proceed forward whereas shorter molecules moved forward unhindered, thereby achieving separation (reprinted with permission from Ref. 38. Copyright 2001 American Chemical Society).

molecules in 15 s with a resolution of ~ 13% (**Fig. 1.2**).[42] The authors discovered that separation depended on pulse duration; however, the correlation between them was not clear. Similarly, using a self-assembled colloidal nanoarray (330 nm silica beads), Zeng showed separation of four DNA fragments in the range of 2-50 kbp.[43] This work furthered the understanding of size and frequency dependency of separations using a DNA prism, and presented guidance for choosing proper conditions to separate DNA of certain sizes.

Clogging and hooking onto the posts are two common problems associated with using nanopillars for pulsed-field electrophoresis of DNA. Also, DNA molecules do not always stay uniformly extended in a hexagonal array and, thus, do not always retrace the same paths. More studies are required to address these issues.

DNA electrophoresis in a direct current electric field. Early work established the foundation of using micro/nanopillar arrays to replace gels or polymers for fractionating DNA molecules in a dc field by measuring their electrophoretic mobilities as a function of length.[26,41] Later, Baba *et al.* demonstrated two types of separations using different nanostructures.[44] The first sieve type nanostructure (S-type) had a regular pillar array (150 nm diameter, 100 nm spacing). Experiments showed smaller molecules moved faster than larger ones in an S-type separation. However, large DNA (48 kbp) became easily clogged in this sieve and sometimes were fragmented by hooking on to pillars. To solve these problems, a second type of structure wasdeveloped on the basis of SEC (SEC-type). This structure was constructed of narrow and wide gaps (400 nm narrow gaps and 1070 nm wide gaps). Molecules smaller than the narrow gaps diffused into both gaps, while molecules larger than the narrow gaps could not enter them and, thus, moved only through the larger gaps. As a result, the larger molecules eluted first, followed by the smaller ones. The SEC-type structure solved clogging and breakup problems

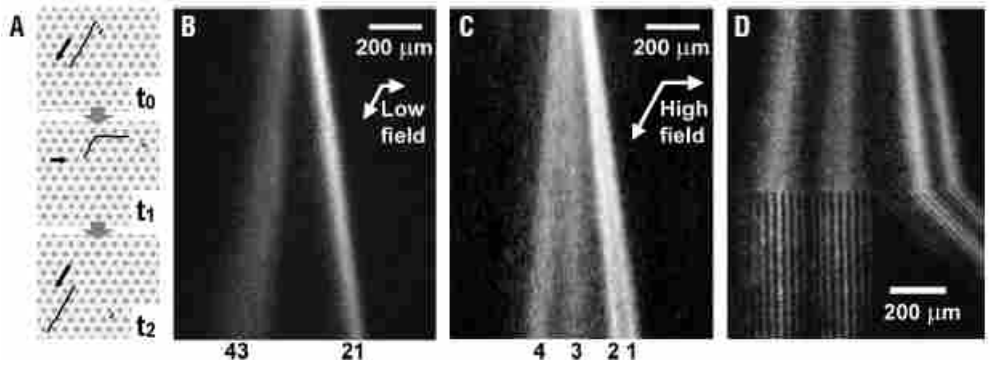

Figure 1.2 (A) Schematic diagram showing the behavior of small and large DNA molecules in a DNA prism under asymmetric fields. At t_0, small and large molecules move at the same speed in a high field. Then at t1, their migration directions are reversed along a low field rotated at 120˚. When the original field is reapplied at t2, the large molecule resumes its previous path while the small molecule starts a new path. (B-D) Fluorescence images of continuous DNA separation under different field strengths and frequencies. Four DNA species were used, including (1) 61 kb, (2) 114 kb, (3) 158 kb and (4) 209 kb. (B) DNA separation into only two bands under a low field. (C) Fully resolved DNA separation using a high field. (D) DNA sample fractions collected through different channels into different reservoirs (reprinted by permission from Macmillan Publishers Ltd: Nature Biotechnology Ref. 42, copyright 2002).

because large DNA could move smoothly through the wide gaps. Using these devices, DNA molecules with sizes of 2, 5 and 10 kbp were clearly separated into bands.

Nanopillar structures inside a microchannel have proven their performance as novel sieving matrices. Unlike conventional DNA electrophoresis, where long DNA can only be separated in an alternating field, quartz-made nanopillar (500 nm diameter, 1 μm spacing) channels were used to fractionate 48.5 and 165.6 kbp DNA in a 380-μm-long region in 10 s using 100 V/cm (**Fig. 1.3**).[45] It was confirmed that smaller molecules moved faster than larger ones, indicating that the nanopillars worked as a sieving matrix. Interestingly, it was discovered that efficient separations could be achieved by adjusting the nanopillar diameter and spacing based on the gyration radii of the DNA molecules. Many other factors, such as nanopillar geometry and array patterns, affect the performance of nanopillar chips. Simulations and experimental results showed that suppression of electroosmosis was a crucial factor in achieving high resolution.[46] For fixed pillar diameter and spacing, two different distributions of nanopillars, tilted and square, were studied.[47] Conformational changes in the DNA were observed in arrays with a square distribution, however, no separation was achieved. Nanopillars with a tilted distribution worked effectively as sieves for size separation of DNA. It was concluded that reptile behavior of DNA[48,49] in nanopillar arrays was an important factor for successful separation. Nanopillar arrays with a hexagonal configuration embedded in a microchannel were reported for long DNA separation in microchip capillary electrophoresis.[50-52] A novel nanofence array provided the same resolving power of a hexagonal nanopost array by ensuring efficient collision between the molecules and the posts, and further improvement in resolution was expected.[53]

A variety of simulations and experimental studies have been conducted on the separation

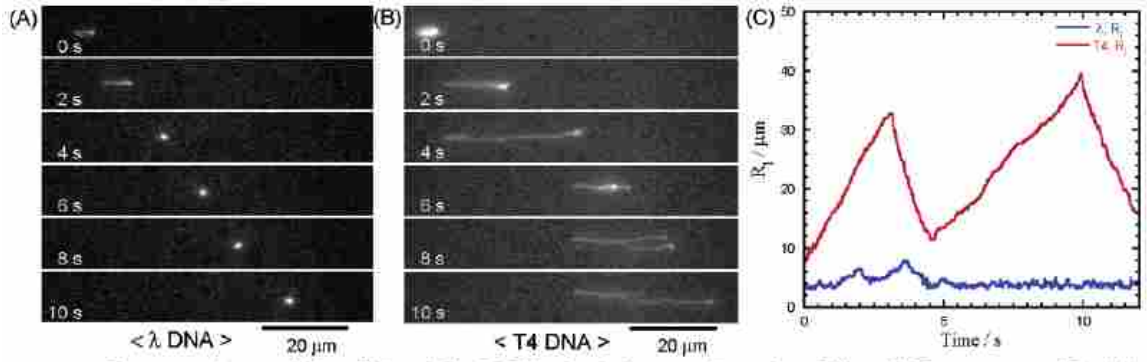

Figure 1.3 Fluorescence micrographs showing the migration of single (A) λ DNA and (B) T4 DNA in a 500-nm-spaced nanopillar channel at 7 V/cm. (C) Plot of the horizontal DNA radii (Rl) versus time, which indicates that T4 DNA formed a U-shape while λ DNA retained a spherical conformation (reprinted with permission from Ref. 45. Copyright 2004 American Chemical Society.).

mechanisms in micro/nanopillar arrays.[54-59] An excellent discussion of these various models is given in a review by Dorfman.[60] The general theory is that, in a post array, when the spacing between the obstacles is smaller than R_g, DNA separation takes place by biased reptation.[61] When the spacing is larger than R_g, the separation is affected by the collisions between the molecules and the posts, which induce conformational changes.[57-59]

1.2.2 Diffusion sorting (Brownian ratchets)

Brownian motion is the random movement of particles in a solution. By taking advantage of the fact that molecules diffuse laterally as they migrate, Duke and Austin[62] and Ertas[63] proposed that a regular lattice of asymmetric obstacles can be constructed to permit Brownian motion essentially in only one direction, guiding the diffusing molecules in specific directions depending on their diffusion coefficients (**Fig. 1.4**). Since small molecules diffuse faster than large molecules, a mixture of particles can be sorted based on size.

There are two types of Brownian ratchets: thermal (also referred to as one-dimensional time-dependent) and steric (also referred to as two-dimensional geometrical). In a thermal ratchet, the particles are subjected to a time-varying asymmetric potential. When the potential is switched on, the particles are driven by electrophoretic force or pressure;[64] whereas, when the potential is switched off, the particles diffuse freely. This approach has been demonstrated as an effective method to separate particles according to size.[65-67] On the other hand, in a steric ratchet (developed by Duke and Austin, and Ertas), particles are driven by a time-independent potential where D is the particle diffusion coefficient, υ is the electrophoretic drift velocity and a is the barrier gap size. It was suggested that, for a particular array geometry (rectangular obstacles set at an angle of 45º to the direction of the applied potential), good resolution could be obtained in the range of $0.02 < D/\upsilon a < 0.3$. Experiments showed that ~100 kbp DNA molecules[68,69] and

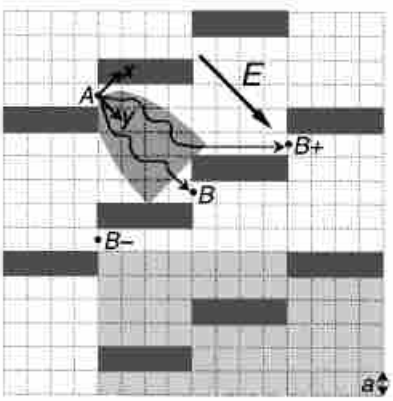

Figure 1.4 Schematic diagram showing how diffusion sorting works in a sieve consisting of a regular lattice of rectangular obstacles. Molecules are driven by an electric field. A molecule which passes gap A visits the parabolic shaded area and subsequently goes to B or B+. Small, fast-diffusing molecules have a higher probability of reaching B+ than large molecules (reprinted with permission from Ref. 62. Copyright 1998 by The American Physical Society.).

phospholipids[70] could be fractionated in such devices. However, there was a discrepancy between the theoretical and experimental D/va values. Later, it was discovered[71] that particles much smaller than the barrier gap were poorly fractionated. An array with a gap size of 1 μm failed to deflect DNA molecules ten times smaller (411 bp, 117 nm). Effective fractionation in asymmetric arrays requires the molecular size to be comparable to the barrier gap size.

One of the limitations of the Brownian ratchet technique is that it is an inherently slow process because it relies on diffusion, and only a low flow rate (2 μm/s) can be used. Furthermore, particles must be injected at the same point, so the overall throughput is low. In order to reduce the analysis time and improve the performance of a ratchet with a given array geometry, the electrophoretic flow direction was tilted at a small angle relative to the array axis (**Fig. 1.5**), which resulted in higher fractionation speed because more diffusing molecules were ratcheted at each step in the array. Using a 12-mm-long array, DNA molecules of 48.5 and 164 kbp were separated with resolution and speed improvements of 3 and 10 times, respectively.[72]

In principle, Brownian ratchet arrays are not limited to DNA separations, but should also be applicable to proteins. Electron-beam lithography and nanoimprint lithography can produce features as small as 10 nm,[20] which is on the same order of magnitude as the size of proteins. However, such small pathways can be easily clogged. Therefore, the practicality of applying this technique to separate proteins is questionable.

In addition to diffusivity-dependent ratchet systems, recent studies have shown that molecules with the same D/va, but different molecular structures, can be separated by combining the self-spreading phenomenon[73,74] with the Brownian ratchet mechanism. Without requiring an external bias, Motegi *et al.*[75] demonstrated the use of a self-spreading lipid bilayer to induce different diffusivities in protein complexes (CTB-GM1) that had different configurations. They

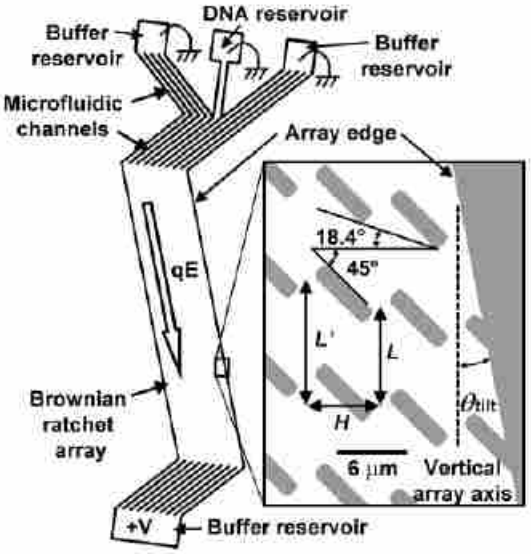

Figure 1.5 Schematic diagram illustrating a Brownian ratchet device in which the electrophoretic flow direction is tilted at an angle of θ_{tilt} with respect to the array axis to achieve higher fractionation speed (reprinted with permission from Ref. 72. Copyright 2003 American Chemical Society.).

proposed a new geometrical model to explain the exceptionally high D/va value and high separation angle observed.

1.2.3 Deterministic lateral displacement (DLD)

This method of separation was first developed by Huang *et al.*[76] and utilizes the asymmetric bifurcation of laminar flow through an array of obstacles to separate particles by their hydrodynamic sizes. In a DLD device, each row of obstacles is slightly offset laterally with respect to the previous row to create equivalent migration paths for all particles of a given size (**Fig. 1.6**). The basic separation principle is called "bumping." Particles smaller than a critical size follow the fluid flow direction and travel in a zigzag mode, whereas particles larger than the critical size are deflected by the post array and eventually become laterally displaced (displacement mode). The critical size, D_c, at which the transition between the two modes occurs, was empirically deduced by Davis[77]

$$D_{c,n} = 1.4dN_n^{-0.48} \quad (1.2)$$

where d is the spacing (center to center) between the posts, N_n is the periodicity, given by $N_n = 1/\Delta_n$ (Δ_n is the relative shift between the adjacent rows). The angle at which the particles are deflected can be calculated as $\tan^{-1}(\Delta_n/d)$.[78]

The difference between the Brownian ratchet and DLD mechanisms is that for a Brownian ratchet, separation depends on diffusion and, thus, only works for small particles such as proteins and DNA, which are affected by Brownian motion, whereas in a bump array, separation depends on a deterministic process (hydrodynamic effects), and higher flow velocity can be used to achieve better resolution. Using a bump array, Huang *et al.*[76] demonstrated that both hard spheres (polystyrene beads) and soft spheres (bacterial artificial chromosomes) were fractionated rapidly with a resolution as low as 10 nm, which is better than hydrodynamic

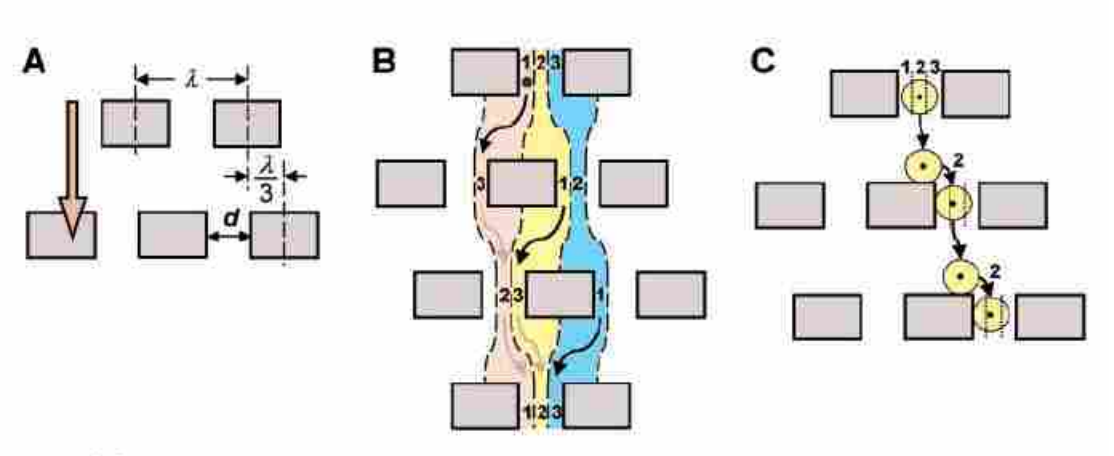

Figure 1.6 Mechanisms of particle separation via deterministic lateral displacement (DLD). (A) In a DLD device, each row of obstacles is slightly offset laterally with respect to the previous row. (B) Small particles follow the laminar flow streams and stay in the same lane. (C) Large particles are continuously deflected by the post array and become laterally displaced (From Ref. 76. Reprinted with permission from AAAS).

chromatography and quasi-elastic laser light scattering. Based on this work, Davis *et al.*[79] investigated three different types of arrays: single array, chirped array and cascade array, each of which has a different mode of separation and a different dynamic range (maximum particle size that can flow through the array without clogging). White blood cells, red blood cells, platelets and plasma were successfully separated from whole blood with no dilution at flow velocities of 1000 μm/s and volumetric flow rates up to 1 μL/min. Since then, cell sorting has become a major application of DLD devices.[78,80-86] In addition to polymer beads, DNA and cells, the technique has also been used for continuous-flow separation of bacteria,[87] fungal spores[88] and parasites.[89] These objects cover a broad size range from 100 nm[90] to 30 μm.

For separation of samples with a broad size distribution, Beech and Tegenfeldt[91] demonstrated a DLD device fabricated from polydimethylsiloxane (PDMS) which could be deformed to change the critical size during the separation. Recently, Loutherback *et al.*[92,93] reported that changing the post shape from circular to triangular increased the dynamic range of DLD arrays. For the same gap width, an array using triangular posts could separate smaller particles, thereby reducing clogging. Circular post arrays use a single-direction flow, while triangular post arrays use an oscillating flow. In addition to the two transport modes discovered for the circular post array, a third possible behavior was observed only in an array with triangular posts. When a particle fell between two critical sizes, it underwent a net displacement relative to the flow after one cycle of flow direction, whereas a particle outside that window showed no net displacement. It was recommended that triangular instead of circular posts should be employed for future DLD designs. Novel operating conditions could include the integration of dielectrophoresis[94] or gravity.[95]

1.3 Nanoplane gap structures

1.3.1 Entropic trapping and Ogston sieving

As mentioned briefly earlier, when the mean pore size is commensurate with the radius of gyration of a DNA molecule ($a \approx R_g$), the sieving process is in the entropic trapping regime. When a flexible DNA molecule is placed in an environment containing different-sized pores, there is a competition between distribution of the chain among different pores and squeezing of the entire chain into a single pore. In order to squeeze into a narrow region, the DNA molecule must overcome an entropic energy barrier resulting from the limited configurational freedom as it passes through. The concept of entropic trapping was first reported in the context of gel electrophoresis.[96] However, the theoretical results from these studies also apply directly to micro/nanostructures.[97]

Although entropic trapping exists in micropillar arrays,[40,98] nanoplane gap structures are more suitable for studying the mechanism because the thin entropic traps can be easily microfabricated to the sizes of the DNA molecules, which are typically in the sub-100 nm range.[99] Han *et al.* demonstrated entropic trapping of long DNA in a dc field using a structure consisting of thousands of alternating shallow (d_s = 90 nm) and deep (d_d = 1 μm) regions.[100] A unique aspect of this type of entropic trapping is that the electrophoretic mobilities of DNA molecules increase with molecular weight. Molecules overcome the energy barrier by stretching through the constrictions. Longer molecules move faster because they have a larger contact area with the thin gap regions and have higher probability of forming a loop and escaping.

In a nanofilter array, the separation resolution depends on the electric field strength. At very low electric fields, the electrophoretic force is not strong enough to help molecules overcome the entropic energy barrier. Therefore, DNA molecules are trapped indefinitely. This

fact can be used to control sample injection.[39] Low fields provide better resolution, but lead to slow separation.[101,102] In order to perform parallel analyses, a device with two identical nanofilter arrays (15 mm long, d_s = 75–100 nm, d_d = 1.5–3 μm) was fabricated. Two different DNA samples (5–50 kbp) were analyzed simultaneously in ~30 min.[101] Unlike traditional PFGE where only a low dc range (1–10 V/cm) can be used, separation was still observed at 128 V/cm.

In entropic trapping, the conformational freedom of the molecules is limited and they must deform to pass through the thin gap regions.[98,103] On the other hand, in Ogston sieving, the molecules retain their coiled conformations as they move through the pores (**Fig. 1.7**). However, their configurational freedom is limited due to steric repulsion from the wall. This results in a configurational entropic energy barrier, which the molecules must overcome in order to pass through any shallow regions.[104] Small molecules move faster than large molecules in an Ogston sieve. Using a nanofilter array, size separation of SDS-protein complexes (cholera toxin subunit, 11.4 kDa; lectin phytohemagglutinin-L, 120 kDa; and low density human lipoprotein, 179 kDa) was achieved in 4 min with a separation length of 5 mm at 90 V/cm, and small DNA molecules (50-766 bp) were fractionated in 10 min at 70 V/cm.[105] Fu *et al.* demonstrated the distinct transition from Ogston sieving to entropic trapping using DNA molecules in the size range from 0.5–8 kbp in a d_s = 73 nm nanofilter array. It was clearly shown that, in the Ogston sieving region, the mobility decreased as the molecular weight increased; in the entropic trapping regime, the mobility increased with DNA length.[106] Compared to other miniaturized systems,[42] DNA analysis using a nanofilter array has the disadvantages of slow separation and, hence, low throughput. A separation can take up to hours, although it is still much faster than conventional PFGE.

The sample processing rate can be increased by simply upscaling the channel depths to

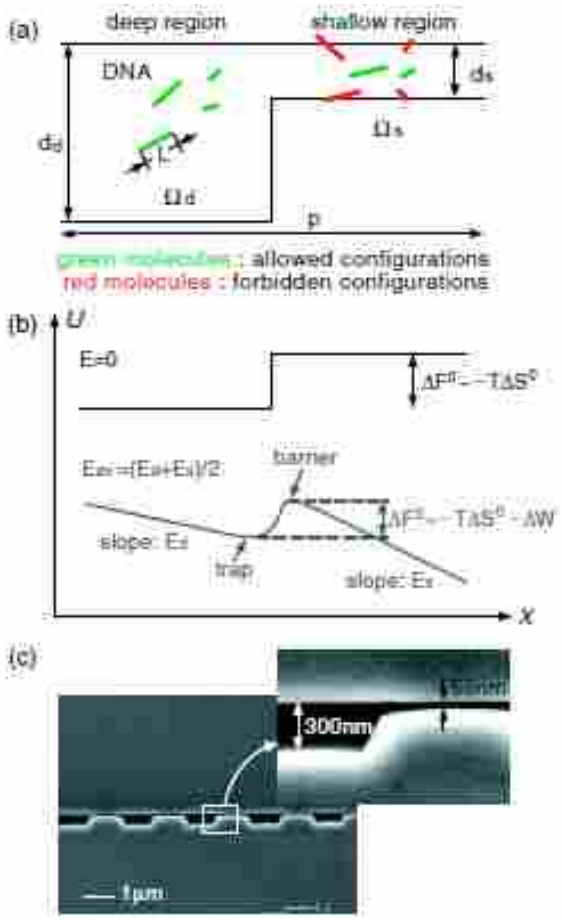

Figure 1.7 (a) Schematic diagram illustrating the partitioning of rod-like DNA molecules between the deep and shallow regions of a nanofilter. (b) Free-energy landscape of a DNA molecule as it moves across a nanofilter. (c) SEM image of a nanofilter consisting of alternating deep (300 nm) and shallow (55 nm) regions of equal length (1 μm) (reprinted with permission from Ref. 106. Copyright 2006 by The American Physical Society.).

create high aspect ratio (depth-to-width ratio) nanochannels.[107] Anisotropic KOH etching provided an attractive method for fabrication of such nanochannels.[108] In order to resolve the low volume throughput limitation, Fu *et al.* developed a two-dimensional anisotropic nanofilter array (ANA) operated with two orthogonal electric fields for continuous-flow separation.[109] The structural anisotropy in the 2D nanofilter caused molecules of different size, charge or hydrophobicity to follow different trajectories. Broad size ranges of DNA (50 bp – 23 kbp) and proteins (10 – 400 kDa) were fractionated in a few minutes. Both entropic trapping and Ogston sieving were demonstrated.[107,109,110]

1.3.2 Size exclusion separation

The concept of size exclusion applies to situations where particles are not able to pass a restriction due to steric hindrance and become excluded by size. DNA molecules can elongate and reptate through pores smaller than their R_g. However, rigid polymer beads, viruses and proteins in their natural states usually cannot be separated via entropic trapping or by a reptation mechanism. Some interesting systems were designed on the basis of size exclusion for trapping and separation of these target analytes.

PDMS nanochannels with tunable cross-sections permit multiple modes of nanofluidic sieving and trapping within a single device for a given sample.[111] Reversible channel deformation provided size selectivity; when a force was applied, the channel trapped particles consistent with the cross-sectional size, and the particles were released upon removal of the applied force. A simple method to operate nanofluidic devices without the use of an external field utilized capillary action and evaporation effects to drive flow inside the channels.[112] The structures consisted of an array of parallel planar nanochannels. Each channel contained one or two height steps. The tall segments were below 200 nm and the short segments were in the range

of 10–100 nm, according to the size distribution of the sample to be analyzed. The trapping of 120 and 30 nm polymer beads and virus capsids was demonstrated. One limitation of the technique is that capillary action was not sufficient to overcome the configurational entropic barrier imposed by Ogston sieving. The channels were easily clogged due to the keystone effect. Surfactant and AC agitation were required in order to reduce channel clogging.[113] However, it was concluded that this one-dimensional design was not suitable for separating complex mixtures. A very similar size fractionation method was reported using a single micro/nanochannel containing a height step. The operating principle was based on application of shear-driven flow, which was generated by mechanically moving the bottom half of a flat-rectangular channel past the top half.[114, 115] Size separations of mixtures of polymer beads and cells were demonstrated.

Stavis *et al.* presented the first three-dimensional nanofluidic structure with the ability to resolve nanoparticle size differences.[116,117] This structure took advantage of the "binning" mechanism, where particles with diameter, D, in the range of $d_s < D < d_d$ were excluded from regions with depths $d \leq d_s$. Proof-of-principle experiments demonstrated the size separation capability of structures with staircase function surface topographies. A prototype device had a maximum depth of ~ 620 nm, a minimum depth of ~ 80 nm, and an average step size of ~ 18 nm. A bimodal nanoparticle mixture was separated in ~ 10 s within a 100-μm channel width. The nanoscale confinement effects on DNA were also investigated. The separation resolution was defined by the nanofluidic step size, which could be further improved via patterning narrower steps.

1.4 Artificial nanoporous membranes

Membrane permeation is a simple and easy-to-implement technique for particle separation. It has been widely used for gas separation, sample filtration/preconcentration and sensing.[118-120] The transport selectivity of a membrane can be engineered for different properties including charge, size and chemical interactions. An ideal membrane-based "molecular filter" should have uniform pore-size distribution throughout the entire thickness of the membrane, allow high analyte flux and have good mechanical and chemical stability. Depending on the relationship between the membrane thickness and pore size, nanoporous membranes can be categorized into two types: nanochannel arrays, if the membrane thickness is larger than the diameter of the pores, and nanopores or nanosieves, if the membrane thickness is on the same order as (or smaller than) the pore diameter. Nanochannels typically are more mechanically robust, whereas nanopores are characterized by lower flow resistance and higher flux.

The production of membranes via track-etching techniques (i.e., irradiation or chemical etching) was proposed approximately a half century ago.[121] Track-etched polymeric membranes have a very narrow pore size distribution. The pore diameter can range from 10 nm to tens of micrometers. Jirage *et al.* demonstrated nanofiltration (<2 nm) of the small molecules, pyridine and quinine, by combing track-etched polycarbonate filters with cylindrical 30 nm pores and gold nanotubules. By using sufficiently long plating time, the pore size of the Au nanotubules embedded in the membranes was reduced to less than 1 nm.[122] Kuo *et al.* used nuclear track-etched polycarbonate membrane arrays with pore sizes of 200 nm or 15 nm to interface fluidic layers in a 3D microchip electrophoresis system.[123,124] Separation and selective collection of amino acids were demonstrated. The flexibility of analyte transfer was demonstrated by nonselective and mass-selective transport of dextrans via adjustment of the pore parameters.

Most track-etched membranes are made of polymer with a thickness of, at least, several micrometers.[125] Vlassiouk *et al.* reported a 100 nm thick silicon nitride (SiN) membrane prepared by ion track-etching.[126] The porosity was controlled by the number of irradiating ions, whereas the pore size could be tuned between ~ 10 and 50 nm depending on the etching time. These membranes could differentiate small dyes of different charges and proteins of different sizes.

Micro/nanofabricated membranes have the potential to advance biomolecule separation processes by offering more precisely controlled structures and allowing the optimization of membrane parameters including porosity, pore geometry and pore surface chemistry.[127] The first ultrathin (~10 nm) SiN membrane was created using focused-ion beam (FIB) etching, which gave uniform pores of 25 nm or less than 10 nm.[128] However, this process was too slow for high volume manufacturing. Striemer *et al.* reported the first use of an ultrathin (15 nm) porous nanocrystalline silicon (pnc-Si) membrane with pore sizes from 5 nm to 25 nm for size- and charge-based separations.[129] It was discovered that the pore size could be tuned by varying the annealing temperature, making pnc-Si membranes ideal for size-selective separation of large biomolecules, such as DNA and proteins. Fractionations of gold nanoparticles and proteins were demonstrated with better than 5 nm resolution.[130] Theoretical analysis was performed by comparing the separation results with one- and three-dimensional models of diffusion through 15-nm membranes.[131] The models predicted that the molecularly thin membranes should have better resolution than thicker membranes with the same pore diameters and porosities.

In the work mentioned above, it was observed that SiN membranes only blocked similarly charged molecules and permitted the passage of oppositely charged molecules. Therefore, they can be functionalized to separate similarly sized molecules on the basis of

charge. For instance, using the same fabrication procedures, Osmangeyoglu *et al.* developed a thin (0.7 – 1 μm) nanoporous anodic alumina membrane with pore sizes from 20 nm to 30 nm.[132] Electrostatic sieving was explored for separation of bovine serum albumin (BSA) and bovine hemoglobin (BHb), which have similar molecular weights, but different isoelectric points. At a pH equal to the pI of BSA, the neutral molecules did not interact electrostatically with the membrane surface and diffused through the pores easily, whereas BHb, which has a different pI, diffused more slowly due to interactions with the membrane and the electrical double layer at low ionic strength. The molecular permeability can also be controlled through chemical interactions. Li and Ito characterized the size-exclusion properties of polystyrene-poly(methylmethacrylate) diblock copolymers (PS-b-PMMA) that contained nanopores with 12 nm-ferritin using an electrochemical approach.[133] The nanopores were modified with polyethylene glycol to reduce nonspecific adsorption.

FIB and electron-beam lithography can generate structures with excellent uniformity. However, the processes are expensive and not suitable for large-scale production.[127,134,135] Montagne *et al.*[136] demonstrated an inexpensive fabrication method for SiN membranes by combining block copolymer (BCP) self-assembly and conventional microfabrication techniques. Size-based filtration experiments were conducted with dextrans of different molecular weight, achieving good selectivity. In addition to 2D membranes, Randall *et al.*[137] fabricated 3D membranes shaped as cubes with five porous faces and one open face, and used them for size-selective sampling. Compared to 2D flat membranes, the 3D membranes had a greater surface-to-volume ratio. As these membranes were moved though liquids, they retained nanobeads and cells.

1.5 Nanosieves based on size exclusion

1.5.1 Device design and operation mechanism

I have been working within a group to develop a simple nanosieving method utilizing capillary action. In this work, three types of nanosieving devices were developed and tested, including two-segment nanochannels (channels with two different height segments), three-segment nanochannels (channels with three different height segments) and tapers (channels with monotonically increasing height segments). An individual nanofluidic chip contains an array of two hundred parallel nanochannels. Each channel is approximately 1.2 mm long and 15 μm wide. The spacing between every two nanochannels is approximately 25 μm. There is one reservoir fabricated at the tall end of the channels for sample injection and one formed at the short end of the channels for waste. Both have the size of 8 mm × 0.2 mm × 0.005 mm (length × width × depth). **Fig. 1.8** shows an example of a completed two-segment nanofluidic device, and the microscopic view displays the interface between the tall and short segments.

Separation of particle mixtures using one of the devices is accomplished by placing a drop of microliter-sized sample into the injection reservoir and allowing it to flow through by capillary action (**Fig. 1.9**). Once the channels are filled, particles continue to migrate towards the exit due to carrier liquid evaporation from the channel ends. Particles are separated based on a simple sieving concept that, when the particle size is smaller than the pore size, they pass through the channels with no retention, whereas, when the particle size is larger than the pore size, they are trapped. Filtration of particles on a nanoscale level does not always occur as predicted; even when pores are large enough to pass all particles, some percentage is often retained. This is because the sieving process is essentially a partitioning equilibrium. There exists

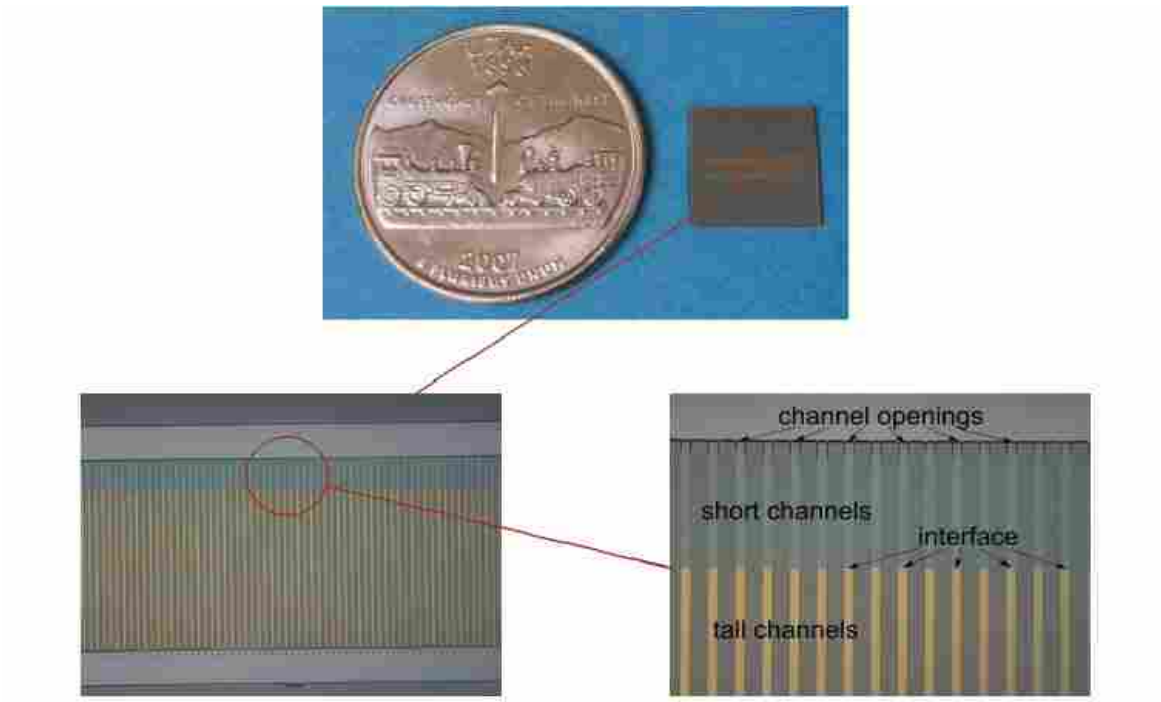

Figure 1.8 (Top) photograph of a completed two-segment device next to a U.S. quarter; (bottom left) microscopic view displaying the nanochannel array and the reservoirs; (bottom right) magnified view showing the interface between tall and short segments.

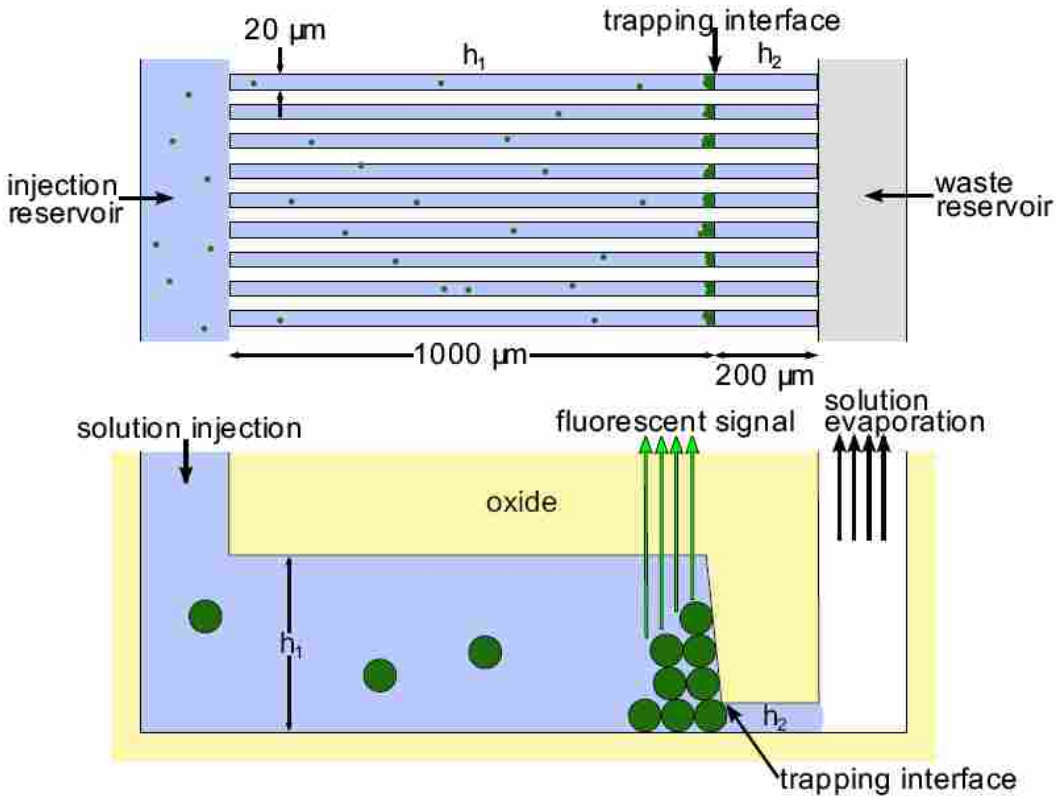

Figure 1.9 Schematic illustrating separation and detection of particles in two-segment nanochannels.

a statistical distribution coefficient, which depends on the molecule size and pore size. This is discussed in detail in later chapters of this dissertation (section 2.3).

Trapping or separation of fluorescently derivatized analytes was recorded with a CCD camera interfaced with a fluorescence microscope (**Fig. 1.9**). Illumination was provided by an LED that passed through a filter cube. Images were acquired sequentially at a rate of 1.33 frames per second. Trapping was quantified by measuring the changes in fluorescence signal intensity for particles accumulated at the interfaces or at the ends of the serially linked nanochannels over the trapping period. Image acquisition and data analysis were performed using Image J software. All trapping data were normalized to the maximum fluorescence intensity. If not otherwise mentioned, each trapping or separation measurement reported in this dissertation was repeated at least two times each using three different nanofluidic chips, for a minimum of 6 total replicates.

1.5.2 Generation of liquid flow

Nanochannels have an extremely large surface-to-volume ratio, which results in prominent capillary action. The wetting properties of the channel walls play a crucial role in the capillary filling of nanochannels. Most reported nanofluidic systems fabricated by micro- and nanolithography are based on hydrophilic materials (silica in this case) and have rectangular cross-sections. The earliest study on capillary phenomena was accomplished by Washburn in the 1920s,[138] which predicted that the position of the moving meniscus during filling (l) is proportional to the square root of the filling time ($t^{1/2}$). However, various studies have shown that the actual capillary flow rate in nanochannels is lower than that predicted theoretically.[139-141] This observation has been attributed to electroviscosity effects,[139,142] or to variation in dynamic contact angle.[143]

The Washburn scaling law is based on the balance between a constant wetting force provided by the capillary pressure, which pulls the liquid into the channels, and a fluidic why resistance that is proportional to the propagated length, L. The Young-Laplace equation can be used to describe the pressure drop across the free surface of the meniscus:

$$\Delta p = \gamma \cdot (1/R_1 + 1/R_2) \tag{1.3}$$

where γ represents the surface tension of the liquid in air, and R_1 and R_2 are the principal radii of curvature. In the case of a planar nanochannel with a rectangular cross-section, where the channel height, h, is much smaller than the channel width, ω, this equation can be converted to

$$\Delta p = 2\gamma \cos\theta / h \tag{1.4}$$

where θ is the contact angle of the liquid on the channel walls. When a channel is filled by water with the surface tension of 0.0728 N/m at 25˚C, and assuming a contact angle of 60˚, the capillary pressure ranges from 7.28 to 72.8 bar for channel depths from 100 to 10 nm.[144-146] The hydraulic resistance, R_h, in a planar nanochannel ($h < \omega$) is given by (μ is liquid viscosity)

$$R_h \approx \frac{12\mu L}{\omega h^3 (1 - 0.630 h/\omega)} \tag{1.5}$$

Therefore, the longer and the shallower the channel is, the higher the flow resistance will be. This is consistent with experimental results, which have shown that capillary filling speed decreases with decreasing channel depth and increasing filling length and is independent of channel width.[147] In this study, the minimum average flow rate obtained was 0.30 mm/s for a 140 nm deep channel and 0.09 mm/s for a 40 nm deep channel (both are 200 μm wide). Since the channel dimensions are in the same range as my devices, it can be assumed that filling of the nanochannels will result in similar flow rate, which is sufficiently high for particle trapping and separation applications. Thus, the nanosieving devices have a significant potential use for pumpless high-speed analysis.

1.5.3 Application scenario: size fractionation of lipoproteins

Lipoproteins are globular particles of varying size and composition, configured in a way that their outer surface is hydrophilic and their inner core, which contains lipids, is hydrophobic. The surface of lipoprotein particles contains an amphipathic phospholipid bilayer, non-esterified cholesterol, and apolipoproteins. The core consists of cholesteryl esters and triglycerides (TG).

One can characterize lipoproteins by their size, density, flotation constant and electrophoretic mobility. Lipoproteins can be separated into five classes based on their size: chylomicron (80-1200 nm), very-low-density lipoproteins (VLDL, 30-80 nm), intermediate-density lipoproteins (IDL, 23-35 nm), low-density lipoproteins (LDL, 18-25 nm) and high-density lipoproteins (HDL, 5-12 nm).[148] These major lipoprotein classes are highly heterogeneous in terms of their density, size and chemical composition, and each consists of two or more subclasses.

HDL are often referred to as "good cholesterol" because they shuttle fat out of the body whereas LDL are referred to as "bad cholesterol" because they deposit cholesterol in the blood vessels. It has been clinically proven that the contents of HDL and LDL in human blood serum are associated with risk of cardiovascular diseases.[149] Because of the clinical significance of lipoproteins, various methods have been used for their quantitative and qualitative analysis. For example, **Fig. 1.10** shows separation profiles of LDL and HDL subclasses obtained by gradient gel electrophoresis (GGE).[150] This is the best resolution that can be achieved using this technique. Obviously, a higher resolution would be preferred. Although gel electrophoresis is widely used, little is understood about how it works on a molecular level because there is little information on the pore sizes of the gels. As an alternative, nanofluidic structures offer a unique opportunity to achieve better resolution and faster separation, and due to the small feature sizes

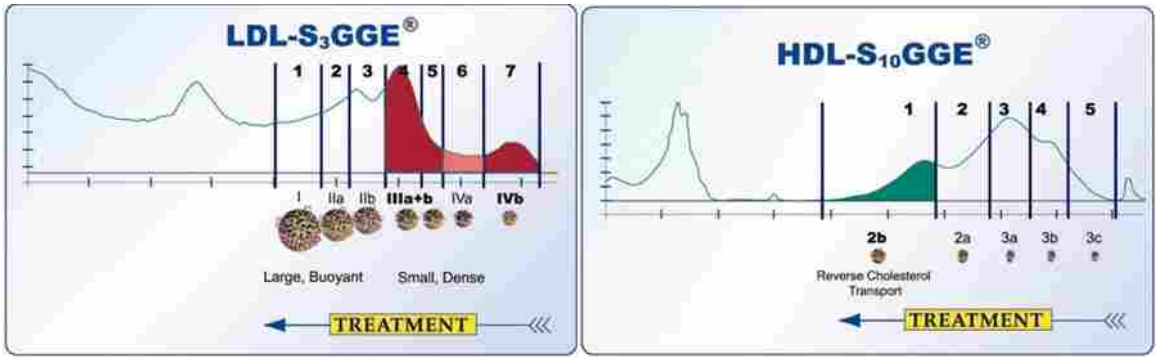

Figure 1.10 Polyacrylamide gradient gel electrophoresis analysis of LDL and HDL subclasses. Image courtesy of Berkeley HeartLab.

in nanofluidic devices, they should further understanding of how sieving works on a molecular level. The ultimate goal of this project was to achieve high resolution size profiles of lipoproteins using tapered nanochannels consisting of multiple heights, monotonically increasing from one side of the channel array to the other. However, due to limited time and the many difficulties and challenges that remain to be overcome, this study only covers trapping and separation of proteins in two-segment nanochannels, and selective trapping of polymer bead mixtures in tapered channels consisting of two different channel heights.

1.6 References

1. Gualfetti, P. J.; Iwakura, M.; Lee, J. C.; Kihara, H.; Bilsel, O.; Zitzewitz, J. A.; Matthews, C. R. *Biochemistry*, **1999**, *38*, 13367-13378.
2. Talmon, Y.; Burns, J. L.; Chestnut, M. H.; Siegel, D. P. *J. Electron. Microsc. Tech.* **1990**, *14*, 6-12.
3. Wen, J.; Arakawa, T.; Philo, J. S. *Anal. Biochem.* **1996**, *240*, 155-166.
4. Kuga, S. *J. Chromatogr.* **1981**, *206*, 449-461.
5. Tiede, K.; Boxall, A. B. A.; Tear, S. P.; Lewis, J.; David, H.; Hasselloov, M. *Food Addit. Contam., Part A* **2008**, *25*, 795-821.
6. Cao, S.; Pollastrini, J.; Jiang, Y. *Curr. Pharm. Biotechnol.* **2009**, *10*, 382-390.
7. Messaud, F. A.; Sanderson, R. D.; Runyon, J. R.; Otte, T.; Pasch, H.; Williams, S. K. R. *Prog. Poly. Sci.* **2009**, *34*, 351-368.
8. Buchholz, B. A.; Doherty, E. A. S.; Albarghouthi, M. N.; Bogdan, F. M.; Zahn, J. M.; Barron, A. E. *Anal. Chem.* **2001**, *73*, 157-164.
9. Hatch, A.V.; Herr, A. E.; Throckmorton, D. J.; Brennan, J. S.; Singh, A. K. *Anal. Chem.* **2006**, *78*, 4976-4984.
10. Zeng, Y.; Harrison, D. J. *Anal. Chem.* **2007**, *79*, 2289-2295.

11. Szumski, M.; Buszewski, B. *Crit. Rev. Anal. Chem.* **2002**, *32*, 1-46.

12. Nge, P. N.; Rogers, C. I.; Woolley, A. T. *Chem. Rev.* **2013**, *113*, 2550-2583.

13. Mukhopadhyay, R. *Anal. Chem.* **2006**, *78*, 7379-7382.

14. Schoch, R. B.; Han, J.; Renaud, P. *Rev. Mod. Phys.* **2008**, *80*, 839-883.

15. Sparreboom, W.; van den Berg, A.; Eijkel, J. C. T. *Nat. Nanotechnol.* **2009**, *4*, 713-720.

16. Bocquet, L.; Charlaix, E. *Chem. Soc. Rev.* **2010**, *39*, 1073-1095.

17. Daiguji, H. *Chem. Soc. Rev.* **2010**, *39*, 901-911.

18. Chou, S. Y.; Krauss, P. R.; Zhang, W.; Guo, L.; Zhuang, L. *J. Vac. Sci. Technol. B* **1997**, *15*, 2897-2904.

19. Hu, W.; Starveswaran, K.; Lieberman, M.; Bernstein, G. H. *J. Vac. Sci. Technol. B* **2004**, *22*, 1711-1716.

20. Guo, J. *Adv. Mater.* **2007**, *19*, 495-513.

21. Jeong, J. W.; Park, W. I.; Do, L. M.; Park, J. H.; Kim, T. H.; Chae, G.; Jung, Y. S. *Adv. Mater.* **2012**, *24*, 3526-3531.

22. Stone, H. A.; Stroock, A. D.; Ajdari, A. *Annu. Rev. Fluid. Mech.* **2004**, *36*, 381-411.

23. Craighead, H. *Nature* **2006**, *442*, 387-393.

24. Mark, D.; Haeberle, S.; Roth, G.; von Stetten, F.; Zengerle, R. *Chem. Soc. Rev.* **2010**, *39*, 1153-1182.

25. Dittrich, P. S.; Manz, A. Nat. Rev. *Drug Discov.* **2006**, *5*, 210-218.

26. Volkmuth, W. D.; Austin, R. H. *Nature* **1992**, *358*, 600-602.

27. de Gennes, P. G. *Scaling Concepts in Polymer Physics*, Cornell University Press, Ithaca, NY, 1979, p 163.

28. Smith, S. B.; Aldridge, P. K.; Callis, J. B. *Science* **1989**, *243*, 203-206.

29. Schwartz, D. C.; Koval, M. *Nature* 1989, ***338***, 520-522.

30. Sambrook, J.; Russel, W. *Molecular Cloning*, 3rd ed.; Cold Spring Harbor Laboratory Press: Cold Spring Harber, NY, 2001; Chapter 5.

31. Viory, J. L.; Miomandre, F.; Miquel, M. C.; Caron, F.; Sor, F. *Electrophoresis*, **1992**, *13*, 1-6.

32. Schwartz, D. C.; Cantor, C. R. *Cell* **1984**, *37*, 67-75.

33. Ogston, A. G. *Trans. Faraday Soc.* **1958**, *54*, 1754-1757.

34. Morris, C. J. O. R. *Protides. Biol. Fluids.* **1967**, *14*, 543-551.

35. Rodbard, D.; Chrambach, A. *Proc. Natl. Acad. Sci. U.S.A.* **1970**, *4*, 970-977.

36. Duke, T. A. J.; Austin, R. H.; Cox, E. C.; Chan, S. S. *Electrophoresis*, **1996**, *17*, 1075-1079.

37. Southern, E. M.; Anand, R.; Brown, W. R. A.; Fletcher, D. S. *Nucleic Acids Res.* **1987**, *15*, 5925-5943.

38. Bakajin, O.; Duke, T. A. J.; Tegenfeldt, J.; Chou, C. F.; Chan, S. S.; Austin, R. H.; Cox, E. C. *Anal. Chem.* **2001**, *73*, 6053-6056.

39. Han, J.; Turner, S. W.; Craighead, H. G. *Phys. Rev. Lett.* **1999**, *83*, 1688-1691.

40. Cabodi, M.; Turner, S. W. P.; Craighead, H. G. *Anal. Chem.* **2002**, *74*, 5169-5174.

41. Turner, S. W.; Lopez, P. A.; Craighead, H. G. *J. Vac. Sci. Technol. B* **1998**, *16*, 3835-3841.

42. Huang, L. R.; Tegenfeldt, J. O.; Kraeft, J. J.; Sturm, J. C.; Austin, R. H.; Cox, E. C. *Nat. Biotechnol.* **2002**, *20*, 1048-1053.

43. Zeng, Y.; He, M.; Harrison, D. J. Angew. *Chem. Int. Ed.* **2008**, *47*, 6388-6391.

44. Baba, M; Sano, T.; Iguchi, N.; Lida, K.; Sakamoto, T.; Kawaura, H. *Appl. Phys. Lett.* **2003**, *83*, 1468-1470.

45. Kaji, N.; Tezuka, Y.; Takamura, Y.; Ueda, M.; Nishimoto, T.; Nakanishi, H.; Horrike, Y.; Baba, Y. *Anal. Chem.* **2004**, *76*, 15-22.

46. Kaji N.; Oki, A.; Ogawa, R.; Takamura, Y.; Nishimoto, T.; Nakanishi, H.; Horike, Y.; Tokeshi, M.; Baba, Y. *Isr. J. Chem.* **2007**, *47*, 161-169.

47. Ogawa, R.; Kaji, N.; Hashioka, S.; Baba, Y.; Horike, Y. *Jpn. J. Appl. Phys.* **2007**, *46*, 2771-2771.

48. Lerman, L. S.; Frisch, H. L. *Biopolymers* **1982**, *21*, 995-997.

49. Lumpkin, O. J.; Zimm, B. H. *Biopolymers* **1982**, *21*, 2315-2316.

50. Chan, Y. C.; Lee, Y. K.; Zohar, Y. *J. Micromech. Microeng.* **2006**, *16*, 699-707.

51. Shi, J.; Fang, A. P.; Malaquin, L.; Pepin, A.; Decanini, D.; Viovy, J. L.; Chen, Y. *Appl. Phys. Lett.* **2007**, *91*, 153114(3).

52. Ou, J.; Joswiak, M. N.; Carpenter, S. J.; Dorfman, K. D. *J. Vac. Sci. Technol. A* **2011**, *29*, 011025(5).

53. Park, S. G.; Olson, D. W.; Dorfman, K. D. *Lab Chip* **2012**, *12*, 1463-1470.

54. Patel, P. D.; Shaqfeh, E. S. G. *J. Chem. Phys.* **2003**, *118*, 2941-2951.

55. Mohan, A.; Doyle, P. S. *Phys. Rev. E* **2007**, *76*, 040903(4).

56. Mohan, A.; Doyle, P. S. *Macromolecules* **2007**, *40*, 8794-8806.

57. Nixon, G. I.; Slater, G. W. *Phys. Rev. E: Stat. Phys. Plasmas. Fluids. Relat. Interdiscip. Top.* **1994**, *50*, 5033-5038.

58. Volkmuth, W. D.; Duke, T.; Wu, M. C.; Austin, R. H.; Szabo, A. *Phys. Rev. Lett.* **1994**, *72*, 2117-2120.

59. Salieb-Beugelaar, G. B.; Dorfman, K. D.; van den Berg A.; Eijkel, J. C. T. *Lab Chip* **2009**, *9*, 2508-2523.

60. Dorfman, K. D. *Rev. Mod. Phys.* **2010**, *82*, 2903-2947.

61. Viory, J. L. *Rev. Mod. Phys.* **2000**, *72*, 813-872.

62. Duke, T. A. J.; Austin, R. H. *Phys. Rev. Lett.* **1998**, *80*, 1552-1555.

63. Ertas, D. *Phys. Rev. Lett.* **1998**, *80*, 1548-1551.

64. Matthia, S.; Müller, F. *Nature*, **2003**, *424*, 53-57.

65. Rousselet, J.; Laurence, S.; Ajdari, A.; Prostt, J. *Nature* **1994**, *370*, 446-447.

66. Faucheux, L. P.; Libchaber, A. *J. Chem. Soc., Faraday Trans.* **1995**, *91*, 3163-3166.

67. Bader, J. S.; Hammond, R. W.; Henck, S. A.; Deem, M. W.; McDermott, G. A.; Bustillo, J. M.; Simpson, J. W.; Mulhern, G. T.; Rothberg, J. M. *Proc. Natl. Acad. Sci. U.S.A.* **1999**, *96*, 13165-13169.

68. Chou, C. F.; Bakajin, O.; Turner, S. W. P.; Duke, T. A. J.; Chan, S. S.; Cox, E. C.; Craighead H. G.; Austin, R. H. *Proc. Natl. Acad. Sci. U. S. A.* **1999**, *96*, 13762-13765.

69. Huang, L. R.; Cox, E. C.; Austin R. H.; Sturm, J. C. *Anal. Chem.* **2003**, *75*, 6963-6967.

70. van Oudenaarden, A.; Boxer, S. G. *Science* **1999**, *285*, 1046-1048.

71. Huang, L. R.; Silberzan, P.; Tegenfeldt, J. O.; Cox, E. C.; Strum, J. C.; Austin, R. H.; Craighead, H. *Phys. Rev. Lett.* **2002**, *89*, 178301-178304.

72. Huang, L. R.; Cox, E. C.; Austin, R. H.; Sturm, J. C. *Anal. Chem.* **2003**, *75*, 6963-6967.

73. Nabika, H.; Sasaki, A.; Takimoto, B.; Sawai, H.; He, S.; Murakoshi, K. J. *Am. Chem. Soc.* **2005**, *127*, 16786-16787.

74. Nabika, H.; Iijima, N.; Takimoto, B.; Ueno, K.; Misawa, H.; Murakoshi, K. *Anal. Chem.* **2009**, *81*, 699-704.

75. Motegi, T.; Nabika, H.; Murakoshi, K. *Langmuir* **2012**, *28*, 6656-6661.

76. Huang, L. R.; Cox, E. C.; Austin, R. H.; Strum, J. C. *Science* **2004**, *304*, 987-990.

77. Davis, J. A. *PhD thesis*, Princeton University, 2008, p24.

78. Morton, K. J. *Proc. Natl. Acad. Sci. U.S.A.* **2008**, *105*, 7434-7438.

79. Davis, J. A.; Inglis, D. W.; Morton, K. J.; Lawrence, D. A.; Huang, L. R.; Chou, S. Y.; Sturm, J. C.; Austin, R. H. Proc. *Natl. Acad. Sci.* **2006**, *103*, 14779-14784.

80. Inglis, D. W.; Morton, K. J.; Davis, J. A.; Zieziulewicz, T. J.; Lawrence, D. A.; Austin, R. H.; Sturm, J. C. *Lab Chip* **2008**, *8*, 925-931.

81. Morton, K. J.; Loutherback, K.; Inglis, D. W.; Tsui, O. K.; Sturm, J. C.; Chou, S. Y.; Austin, R. H. *Lab Chip* **2008**, *8*, 1448-1453.

82. Inglis, D. W. *J. Immunol. Methods* **2008**, *329*, 151-156.

83. Green, J. V.; Radisic, M.; Murthy, S. K. *Anal. Chem.* **2009**, *81*, 9178−9182.

84. Joensson, H. N.; Uhlen, M.; Svahn, H. A. *Lab Chip* **2011**, *11*, 1305−1310.

85. Inglis, D. W.; Lord, M.; Nordon, R. E. *J. Micromech. Microeng.* **2011**, *21*, 054024(8).

86. Beech, J. P.; Holm, S. H.; Adolfsson, K.; Tegenfeldt, J. O. *Lab Chip* **2012**, *12*, 1048−1051.

87. Morton, K. J.; Loutherback, K.; Inqlis, D.; Tsui, O. K.; Sturm, J. C.; Chou, S. Y.; Austin, R. H. *Lab Chip* **2008**, *8*, 1448-1453.

88. Inglis, D. W.; Herman, N.; Vesey, G. *Biomicrofluidics* **2010**, *4*, 024109(8).

89. Holm, S. H.; Beech, J. P.; Barrett, M. P.; Tegengeldt, J. O. *Lab Chip* **2011**, *11*, 1326-1332.

90. Morton, K. J.; Sturm, J. C.; Austin, R. H.; Chou, S. Y. *Proceedings of μTAS conference* **2006**, *1*, 1814-1817.

91. Beech, J. P; Tegenfeldt, J. O. *Lab Chip* **2008**, *8*, 657-659.

92. Loutherback, K.; Puchalla, J.; Austin, R. H.; Sturm, J. C. *Phys. Rev. Lett.* **2009**, *102*, 045301(4).

93. Loutherback, K.; Chou, K. S.; Newman, J.; Puchalla, J.; Austin, R. H.; Sturm, J. C. *Microfluid Nanofluid* **2010**, *9*, 1143-1149.

94. Beech, J. P; Tegenfeldt, J. O. *Lab Chip* **2009**, *9*, 2698-2706.

95. Devendra, R.; Drazer, G. *Anal. Chem.* **2012**, *84*, 10621-10627.

96. Arvanitidou, E.; Hoagland, D. *Phys. Rev. Lett.* **1991**, *67*, 1464-1466.

97. Fu, J.; Mao, P.; Han, J. *Trends Biotechnol.* **2008**, *26*, 311-320.

98. Turner, S. W. P.; Cabodi, M.; Craighead, H. G. *Phys. Rev. Lett.* **2002**, *88*, 128103(4).

99. Eijkel, J. C. T.; van den Berg, A. *Electrophoresis* **2006**, *27*, 677-685.

100. Han, J.; Turner, S. W.; Craighead, H. G. *Phys. Rev. Lett.* **1999**, *83,* 1688-1691.

101. Han, J.; Craighead, H. G. *Science* **2000**, *288*, 1026-1029.

102. Han, J.; Craighead, H. G. *Anal. Chem.* **2002**, *74*, 394-401.

103. Nykypanchuk, D.; Stery, H. H.; Hoagland, D. A. *Science* **2002**, *297*, 987.

104. Abgrall, P.; Nguyen, N. T. *Anal. Chem.* **2008**, *80*, 2326-2341.

105. Fu, J.; Mao, P.; Han, J. *Appl. Phys. Lett.* **2005**, *87*, 263902(3).

106. Fu, J.; Yoo, J.; Han, J. *Phys. Rev. Lett.* **2006**, *97*, 018103(4).

107. Mao, P.; Han, J. *Lab Chip* **2009**, *9*, 586-591.

108. Han, J.; Fu, J.; Schoch, R. B. *Lab Chip* **2008**, *8*, 23-33.

109. Fu, J.; Schoch, R. B.; Stevens, A. L.; Tannenbaum, S. R.; Han, J. *Nat. Nanotech.* **2006**, *2*, 121-128.

110. Fu, J.; Schoch, R. B.; Stevens, A. L.; Tannenbaum, S. R.; Han, J. *Nat. Nanotechnol.* **2007**, *2*, 121-128.

111. Huh, D.; Mills, K. L.; Zhu, X. Y.; Burns, M. A.; Thouless, M. D.; Takayama, S. *Nat. Mater.* **2007**, *6*, 4242-428.

112. Hamblin, M. N.; Xuan, J.; Maynes, D.; Tolley H. D.; Belnap, D. M.; Woolley, A. T.; Lee, M. L.; Hawkins, A. R. *Lab Chip* **2010**, *10*, 173-178.

113. Xuan, J.; Hamblin, M. N.; Stout, J. M.; Tolley, H. D.; Maynes, R. D.; Woolley, A. T.; Hawkins, A. R.; Lee, M. L. *J. Chromatogr. A* **2011**, *1218*, 9102-9110.

114. Vankrunkelsven, S.; Clicq, D.; Pappaert, K.; Baron, G. V.; Desmet, G. *Anal. Chem.* **2004**, *76*, 3005-3011.

115. Vankrunkelsven, S.; Clicq, D.; Pappaert, K.; Ranson, W.; De Tandt, C.; Ottevaere, H.; Thienpont, H.; Baron, G. V.; Desmet, G. *Electrophoresis* **2004**, *25*, 1714-1722.

116. Stavis, S. M.; Strychalski, E. A.; Gaitan, M. *Nanotechnology* **2009**, *20*, 165302(7).

117. Stavis, S. M.; Geist, J.; Gaitan, M. *Lab Chip* **2010**, *10*, 2618-2621.

118. Pandey, P.; Chauhan, R. S. *Prog. Polym. Sci.* **2001**, *26*, 853-893.

119. Long, Z.; Liu, D.; Ye, N.; Qin, J.; Lin, B. *Electrophoresis* **2006**, *27*, 4927-4934.

120. Stroeve, P.; IIeri, N. *Trends Biotechnol.* **2011**, *29*, 259-266.

121. Apel, P. *Radial. Meas.* **2001,** *34*, 559-566.

122. Jirage, K. B.; Hulteen, J.; Martin, C. R. *Science* **1997**, *278*, 655-658.

123. Kuo, T.; Cannon, D. M.; Chen, Y.; Tulock, J. J.; Shannon, M. A.; Sweedler, J. V.; Bohn, P. W. *Anal. Chem.* **2003**, *75*, 1861-1867.

124. Kuo, T.; Cannon, D. M.; Shannon, M. A.; Bohn, P. W.; Sweedler, J. V. *Sens. Actuat. A* **2003**, *102*, 223-233.

125. Savariar, E. N.; Krishnamoorthy, K.; Thayumanavan, S. *Nat. Nanotechnol.* **2008**, *3*, 112-117.

126. Vlassiouk, I.; Apel, P.; Dmitriev, S. N.; Healy, K.; Siwy, Z. S. *Proc. Natl. Acad. Sci.* **2009**, *106*, 21039-21044.

127. Desai, T. A.; Hansford, D.; Ferrari, M. *J. Membr. Sci.* **1999**, *159*, 221-223.

128. Tong, H. D.; Jansen, H. V.; Gadgil, V. J.; Bostan, C. G.; Berenschot, E.; van Rijin, C. J. M.; Elwenspoek, M. *Nano Lett.* **2004**, *4*, 283-287.

129. Striemer, C. C.; Gaborski, T. R.; McGrath, J. L.; Fauchet, P. M. *Nature* **2007**, *445*, 749-753.

130. Gaborski, T. R.; Synder, J. L.; Striemer, C. C.; Fang, D. Z.; Hoffman, M.; Fauchet, P. M.; McGrath, J. L. *ACS Nano.* **2010**, *4*, 6973-6981.

131. Snyder, J. L.; Clark, A..; Fang, D. Z.; Gaborski, T. R.; Striemer, C. C.; Fauchet, P. M.; McGrath, J. L. *J. Membr. Sci.* **2011**, *369*, 119-129.

132. Osmangeyoglu, H. U.; Hur, T. B.; Kim, H. K. *J. Membr. Sci.* **2009**, *343*, 1-6.

133. Li, Y.; Ito, T. *Anal. Chem.* **2009**, *81*, 851-855.

134. Srijanto, B.; Retterer, S.; Fowlkes, J. D.; Doktycz, M. J. *J. Vac. Sci. Technol. B* **2010**, *28*, 48-52.

135. Kim, M. J.; Wanunu, M.; Bell, D. C.; Meller, A. *Adv. Mater.* **2006**, *18*, 3149-3155.

136. Montagne, F.; Blondiaux, N.; Bojko, A.; Pugin, R. *Nanoscale* **2010**, *4*, 5880-5886.

137. Randall, C. L.; Gillespie, A.; Singh, S.; Leong, T. G.; Gracias, D. H. *Anal. Bioanal. Chem.* **2009**, *393*, 1217-1224.

138. Washburn, E. W. *Phys. Rev.* **1921**, *17*, 273-283.

139. Haneveld, J.; Tas, N. R.; Brunets, N.; Jansen, H. V.; Elwespoek, M. *J. Appl. Phys.* **2008**, *104*, 014309(6).

140. Oh, J. M.; Faez, T.; de Beer, S.; Mugele, F. *Microfluid. Nanofluid.* **2010**, *9*, 123.

141. Hamblin, M. N.; Hawkins, A. R.; Murray, D.; Maynes, D.; Lee, M. L.; Woolley, A. T.; Tolley, H. D. *Biomicrofluidics* **2011**, *5*, 021103(6).

142. Mortensen, N. A.; Kristensen, A. *Appl. Phys. Lett.* **2008**, *92*, 063110(3).

143. Zhu, Y.; Petkovic-Duran, K. *Microfluid. Nanofluid*. **2010**, *8*, 275-282.

144. Batchelor, G. K. *An Introduction to Fluid Dynamics*, Cambridge University Press: Cambridge, England, 1967.

145. Mery, E.; Ricoul, F.; Sarrut, N.; Constantin, O.; Delapierre, G.; Garin, J.; Vinet, F. *Sens. Actuators, B* **2008**, *134*, 438-446.

146. Abgrall, P.; Nguyen, N. T. *Anal. Chem.* **2008**, *80*, 2326-2341.

147. Kuo, J. N.; Lin, Y. K. *Jpn. J. Appl. Phys.* **2012**, *5*, 105201(5).

148. Rifai, N.; Warnick, G. R.; Dominiczak, M. H. *Handbook of Lipoprotein Testing*, AACC Press: Washington DC, 2000**;** p 1.

149. Schaefer, E. J. *Am. J. Clin. Nutr.* **2002**, *75*, 191-212.

150. Warnick, G. R.; McNamara, J. R.; Boggess, C. N.; Clendenen, F.; Williams, P. T.; Landolt, C. C. *Clin. Lab. Med.* **2006**, *26*, 803-846.

Chapter 2. Two-segment nanochannels

2.1 Fabrication

This work describes a set of nanofluidic devices developed using aluminum as sacrificial core. This process is illustrated in **Fig. 2.1** using the example of an array of two-segment channels where the first segments are 200 nm tall and the second following segments are 45 nm tall. The terminology for describing devices like this throughout this dissertation is 200-45 nm channels. The fabrication process begins with depositing approximately 200 nm plasma enhanced chemical vapor deposited (PECVD) silicon dioxide, which will form the wettable bottom of the nanochannels. Then a thin layer of 45 nm aluminum (Al) is deposited on top of the oxide, defining the short segments. Photoresist AZ nLOF 2220 is spun-on, patterned and developed, exposing only an area where a second a layer of 155 nm Al is deposited. The photoresist layer is then lifted off using N-methylpyrrolidone (NMP), leaving behind two aluminum-covered areas of two different heights. Then photoresist AZ 3330 is spun-on, patterned and developed, defining the core lines. After etching out the aluminum between the core lines using a commercial aluminum etchant and removing the photoresist using acetone, the Al core lines are formed. At this step, the channels heights are characterized using profilometry, and a capping layer of approximately 5 μm PECVD is deposited over the core lines. Then AZ 3330 is used to form reservoirs at both ends of the core lines, which are etched out using a buffered oxide etchant (BOE) to expose the cores. By etching away the metal in aqua regia (a 3:1 mixture of hydrochloric acid and nitric acid), hollow channels are created.

It is known that the developer AZ 300 MIF etches aluminum. Therefore, later in the project, I used ~15–20 nm thick chromium (Cr) as a protecting layer on top of Al, which is

deposited in the same electron-beam deposition cycle as Al. The Cr is removed in chrome etchant after photoresist has been developed and before the next layer of aluminum is deposited. Additionally, it should be pointed out that the nanofluidic chips have a variation of ±5 nm in channel heights due to the nature of thermal deposition.

2.2 Trapping of virus capsids

In order to demonstrate the capability of the nanosieving chips to trap biological nanoparticles, I used two types of spherical virus capsids: Herpes Simplex Virus type 1 (HSV-1) and Hepatitis B Virus (HBV). The HSV-1 sample was obtained from the laboratory of J. Brown (University of Virginia) and the HBV sample was obtained from the laboratory of A. Zlotnick (Indiana University).

HSV-1 has an icosahedral capsid with an average diameter of 120 nm.[1] It belongs to the herpes virus family, responsible for a range of illness from cold sores to encephalitis. HBV is the prototype of a family of small hepatotropic viruses causing acute and chronic liver disease. It also has an icosahedral capsid but is smaller, approximately 30 nm in diameter.[2] To facilitate visualization during trapping experiments, for both HSV-1 and HBV, the capsid of the native virus was labeled with FITC. Specifically, a 100 μL purified virus preparation was diluted (1:1 ratio) with labeling buffer (100 mM bicarbonate buffer adjusted to pH 9.0). This virus suspension was incubated with 10 μL of FITC stock solution (~ 2 mM in dimethyl sulfoxide) in a dark room at room temperature for 24 h. To remove excessive FITC and concentrate the sample for trapping, the virus suspension was diluted to 2 mL with 50 mM, pH 8.3 borate buffer and centrifuged at 6000 rpm with an SS-34 rotor for 15 min using centrifugal membrane filters with a cutoff of 30,000 Da. This step was repeated to produce a final volume of 200 μL virus

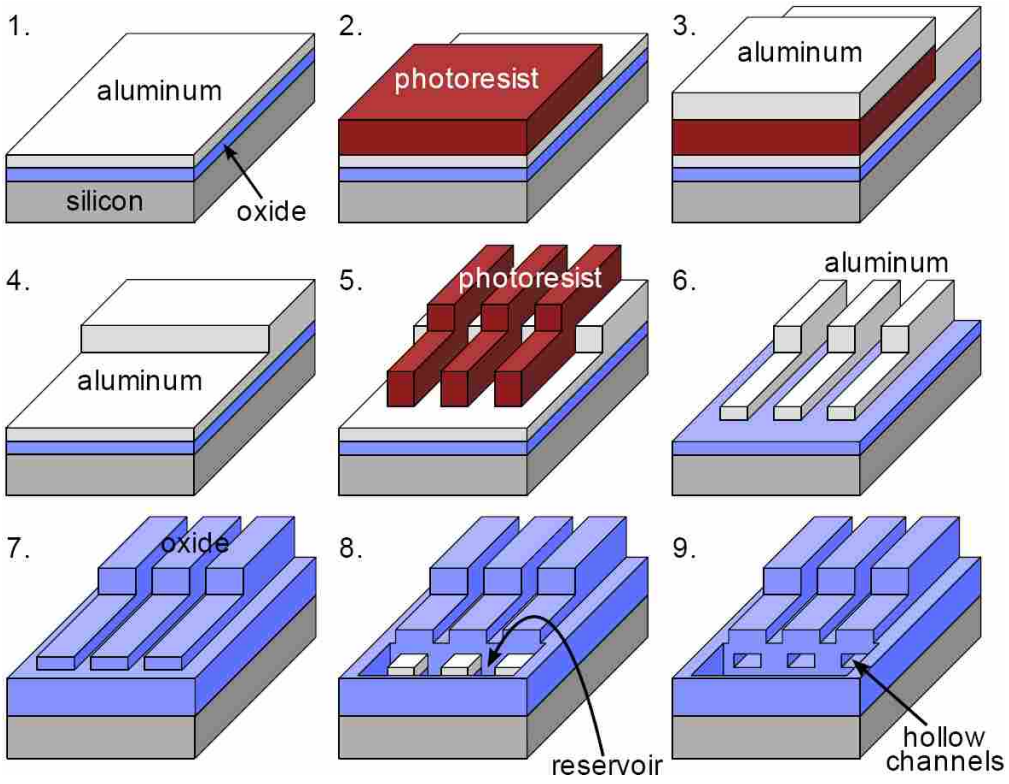

Figure 2.1 Schematic illustrating the fabrication process involved in making two-segment sacrificial nanochannels.

suspension.

For HSV-1 capsids, the viral protein concentration was 2.3 mg/mL as determined from DC protein assay using α-1-antitrypsin as a standard, which corresponds to approximately 5.4×10^{12} particles/mL (the HSV-1 capsid sample contained three types of capsids: type A (200 MDa average MW, 45%), type B (250 MDa average MW, 45%) and type C (300 MDa average MW, 10%). Therefore, the average molecular weight of the capsid mixture was approximately 230 MDa). For HBV capsids, the viral concentration was 6.76 mg/mL as determined from DC protein assay using BSA as the standard, which corresponds to approximately 9.44×10^{14} particles/mL (HBV capsids have a molecular weight of approximately 4.25 MDa).

Before and after the labeling process, microscopy using a transmission electron microscope (Philips Tecnai F30 TEM operated at 300 kV) was performed to ensure that there were no other virus species in the sample, that the derivatized virus retained its original structure, and that the derivatization did not cause aggregation of the viruses. TEM micrographs for HSV-1 capsids and HBV capsids are shown in **Fig. 2.2**, respectively.

To trap the HSV-1 capsids, a 190-65 nm device was used. To trap the HBV capsids, a 145-25 nm device was used. Time lapse photographs showed an increase in fluorescence signal confined to the channel interface over time for both samples (**Fig. 2.3**). No signal was detected at the channel exits, demonstrating successful trapping.

By analyzing how the fluorescent signal changes over time (**Fig. 2.4**), it can be observed that the slope of the HSV-1 curve is steeper than that of the HBV curve before 20 s, indicating faster initial flow rate. Since the 190-65 nm channels used for HSV-1 trapping are taller than the 145-25 nm channels used for HBV trapping, faster filling is expected. Also, other factors can

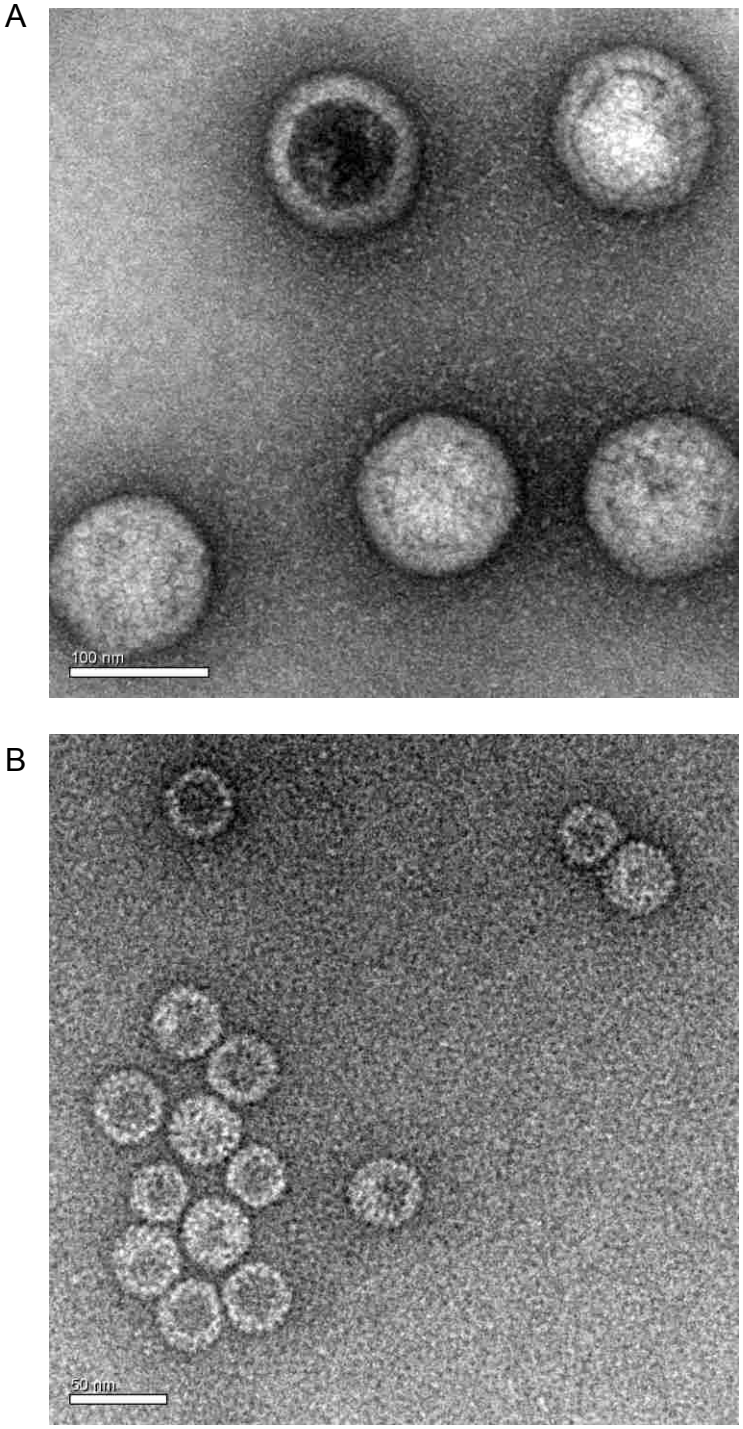

Figure 2.2 TEM images showing (A) FITC-conjugated 120 nm HSV-1 capsids and (B) 30 nm HBV capsids. These images demonstrate that the viral structures remain intact following labeling and purification procedures.

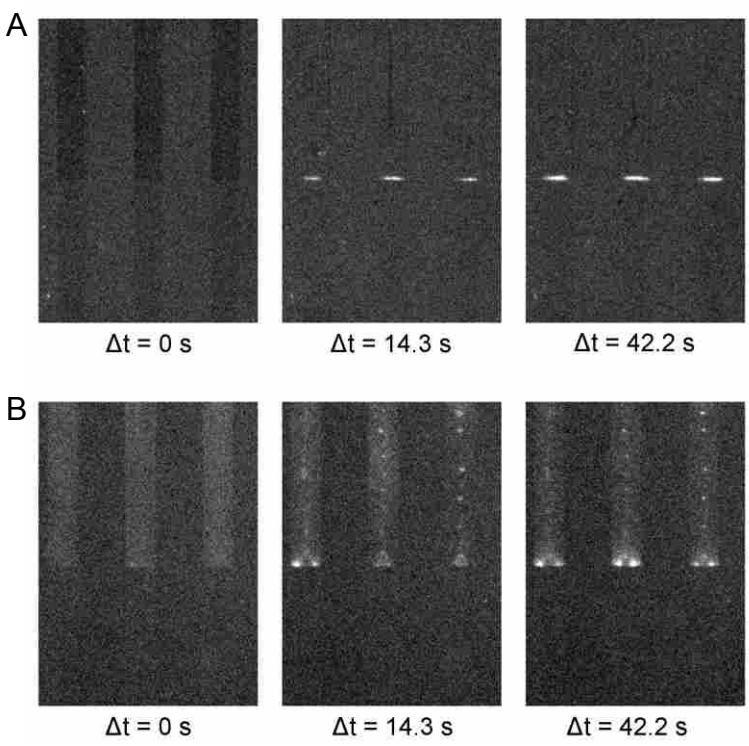

Figure 2.3 Time lapse images of virus trapping. (A) HSV-1 trapping in 190-65 nm channels and (B) HBV trapping in 145-25 nm channels.

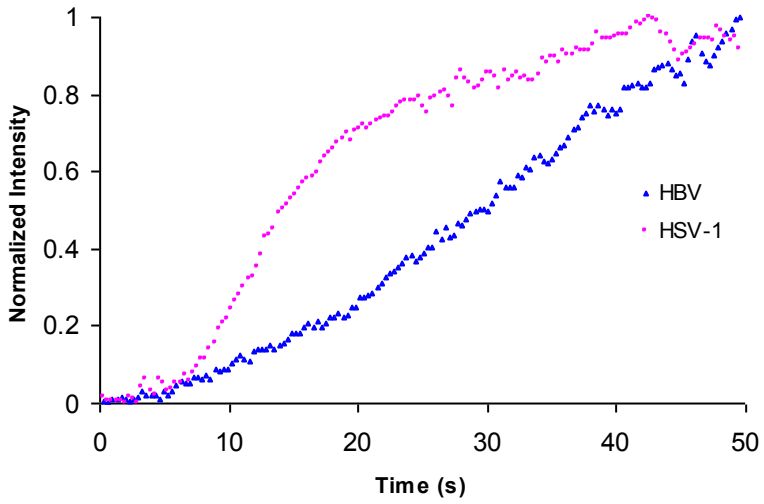

Figure 2.4 Normalized intensity versus time analysis of HBV trapping in 145-25 nm channels and HSV-1 trapping in 190-65 nm channels.

contribute to the results: (a) different surface properties of the two different types of viruses; (b) HBV has a smaller diameter than HSV-1 and therefore, larger surface-to-volume ratio, which can result in a greater chance to interact with the wall; and (c) the devices used for trapping HBV have a larger surface-to-volume ratio than the ones used for trapping HSV-1, which also can lead to more analyte-wall interactions. The hypothesis can be backed up by the more severe nonspecific adsorption observed in the tall segments of 145-25 nm channels than 190-65 nm channels.

2.3 Separation of polymer beads

It has been demonstrated that when the particle size is larger than the pore size, none of the particles are able to pass through the interface. When the particle size is smaller than the pore size, intrinsically, I expected all of the particles to pass without retention. However, when a sample of Chromeon 470 labeled, carboxy-modified 30 nm (nominal size) polyacrylonitrile (PAN) nanobeads (6×10^{12} particles/mL) was introduced into 200-45 nm channels, the nanoparticles were separated into two fractions: one stopping at the 45 nm interfaces and the other passing through the interfaces and migrating to the ends of the channels where they accumulated as the liquid carrier evaporated. By comparing the fluorescence signal intensities and assuming that they were linearly related to the number of trapped particles, the ratio of particle number in these two fractions was approximately 1:1 (**Fig. 2.5**). As mentioned earlier, trapping tests were repeated twice each using three different devices. The distribution ratio was 0.9:1, 1:1, 1.1:1, 1:1, 1.2:1 and 1:1, respectively, with an average of 1:1. Applying the macroscopic concept of filtration, the data indicate that half of the particles are smaller than 45 nm and the other half larger than 45 nm. This is inaccurate because the manufacturer confirmed

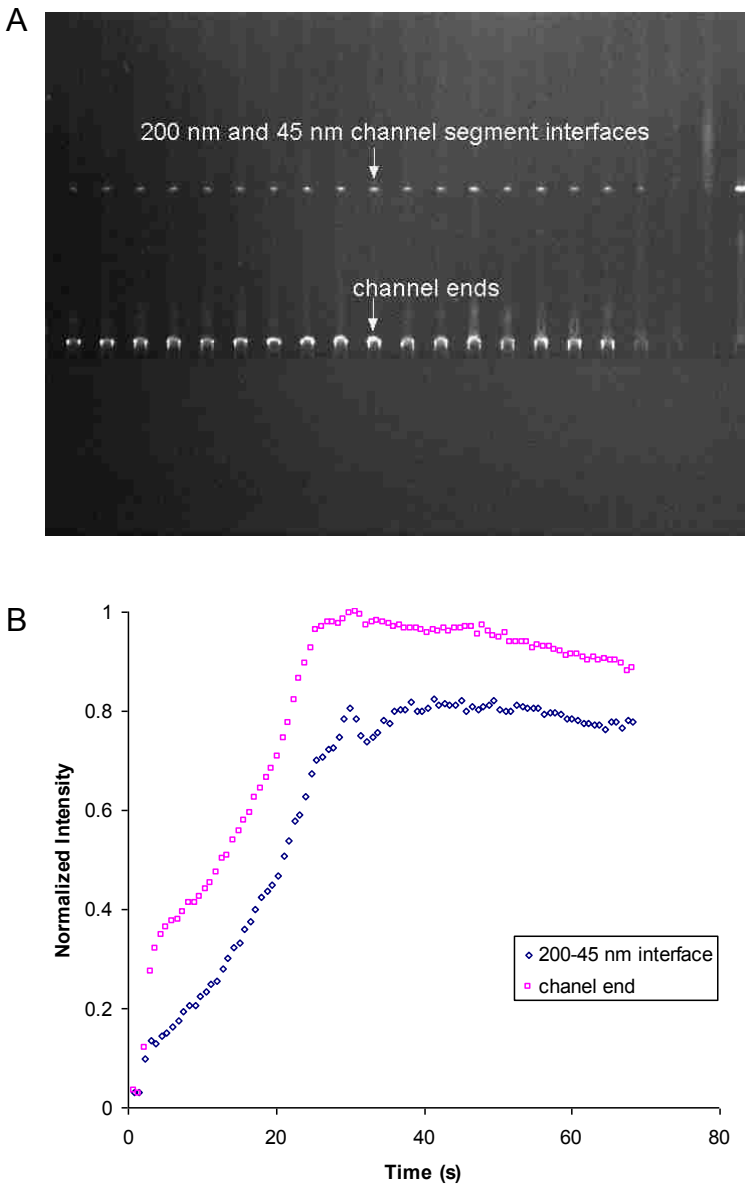

Figure 2.5 (A) Image of a separation of 30–50 nm PAN beads in 200-45 nm channels. (B) Plot (normalized signal intensity versus time) showing that the particles distributed in a 1:1 ratio between the 45 nm barriers and the 45 nm channel exits.

that the majority of the beads had a diameter of 30 nm and all were smaller than 50 nm. There are several possibilities that could lead to the resultant data: (a) agglomeration, which induces channel clogging and prevents particles from passing, (b) "keystone effect," and (c) statistical distribution.

The so-called "keystone effect" is often reported as occurring during the manufacture of particulate packed capillary columns. It was previously observed that, when a capillary column was packed with particles of diameters much smaller than the outlet, instead of being flushed out of the column because of their smaller size, they were retained at the outlet in a similar manner as a "keystone" arch in a stone bridge.[3] For instance, Kennedy and Jorgenson[4] reported that 5 μm particles were lodged in columns of 15-25 μm i.d. during the packing process and could not be moved even at a pressure of 300 bar. Additionally, Lord et al.[5] reported that 3 μm particles were retained in a 20 μm outlet of a capillary electrochromatography column. Similarly, I believe that the keystone effect contributed to the result that particles smaller than 45 nm were immoblized at the interface.

On the other hand, Giddings pointed out that, in size exclusion chromatography, the distribution of particles between the bulk liquid and porous networks is a partitioning process.[6] The equilibrium distribution coefficient K is the ratio of partition functions for molecules within the pores and within the bulk liquid. Consequently, it is a ratio of the configuration integrals

$$K = \frac{\iiint \mathrm{d}\mathbf{r}\mathrm{d}\psi\mathrm{d}\lambda\exp\left[-\epsilon_{\mathrm{p}}(\mathbf{r},\psi,\lambda)/kT\right]}{\iiint \mathrm{d}\mathbf{r}\mathrm{d}\psi\mathrm{d}\lambda\exp[-\epsilon_{\mathrm{b}}(\lambda)/kT]} \tag{2.1}$$

For rigid particles in a pore between two infinite parallel plates, the model becomes

$$K = 1 - d_p/2h \tag{2.2}$$

where d_p is the particle diameter and h is the pore size. Interestingly, even when the pore is larger than the particles to be filtered, some of them will still be excluded. This can be explained from the principles of statistical thermodynamics. In **Fig. 2.6**, certain molecular configurations are forbidden due to the steric repulsion from the pore wall to prevent partial overlap. In this case, exclusion is essentially a surface effect. The loss of configurational entropy from entering a smaller pore results in partial exclusion from such regions.

Based on the Giddings model, the ratio of number of trapped particles to total number of particles should be equal to the ratio of particle diameter to channel height

$$\text{Trapped/total} = d_p/h \text{ (or } T/t = d_p/h) \tag{2.3}$$

where d_p is the particle diameter and h is the barrier height. The value of T/t can be determined by calculating the ratio of fluorescence intensity at the barrier versus the summed fluorescence intensity at the barrier and the exit. According to this model, the separation of 30 nm particles in 200-45 nm channels should result in a trapped/total value of 2:3, whereas the actual ratio was 1/2, indicating that more particles are able to escape the barrier than theory predicts. A new model that incorporates the differences between this device design and Giddings' system to explain the discrepancy is being studied. Currently, it is assumed that the difference is due to utilization of capillary action, which helps particles overcome the entropic energy barrier. Separation is achieved only via diffusion in Giddings' model. This could lead to a smaller trapped/total value. However, it does not necessarily mean that all particles smaller than the barrier height are able to pass. It should be noted in **Fig. 2.5** the slopes of the curves are steepest in the first few seconds when capillary action is taking place. Once capillary action is complete, the separation process slows down (smaller slope) and eventually reaches equilibrium (between 2-32 s), after which particle migration is driven by evaporation from the channel ends.

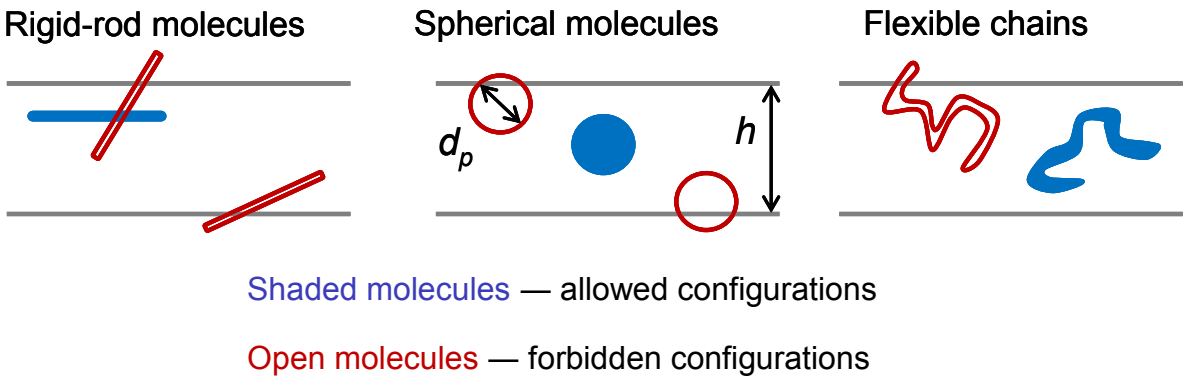

Figure 2.6 Illustration of allowed and forbidden configurations of different shaped particles confined between two infinite parallel planes (adapted from Ref. 6. Copyright 1968 American Chemical Society.).

2.4 Trapping and separation of proteins

2.4.1 Surface deactivation

Polymer beads and even virus particles can be considered to be rigid compared to proteins. One of the major challenges of trapping or separating proteins using silica-based nanochannels is nonspecific interactions between proteins and the wall surface. This is because the surface-to-volume ratio increases substantially when columns or channels move down to nanoscale dimensions, which means that the chance for a protein particle to interact with the surface is also greatly increased. Considering the example of a capillary of 50 μm inner diameter, the surface-to-volume ratio is only 0.08, while for a 40 nm tall, 20 μm wide nanochannel, the ratio is 50, which is a 625-fold increase.

Protein adsorption is a very complex process. It is governed by protein-surface forces, including steric repulsion, van der Waals, electrostatic and hydrophobic interactions.[7] Ionic strength, pH, and properties of the protein and the surface all affect how a protein interacts with a surface. Charged surfaces, such as silica (pH ~ pKa of silanol groups), are typically hydrophilic. In this case, electrostatic interactions are responsible for protein adsorption. Theoretically, by controlling the pH, proteins can bear charges of the same sign as the silanol groups on silica and be repelled from the surface, assuming that these charges are evenly distributed over the protein surface. However, the surface of a protein is not homogeneous. It may possess hydrophobic, hydrophilic, cationic and anionic patches at the same time.[8] Consequently, electrostatic attractions may take place between the oppositely charged patches on the protein surface and the silica walls. Additionally, adsorption induces conformational changes in the protein, which increases the structural entropy. This entropy gain can overcome unfavorable conditions such as electrostatic repulsion. Therefore, the structural stability of proteins is an important factor in

adsorption. “Soft proteins” with low internal stabilities, such as BSA, and human serum proteins are more likely to absorb on surfaces than “hard proteins” with high internal stabilities, such as lysozyme and fibrinogen.[9]

Many studies have been aimed at reducing nonspecific adsorption on different types of surfaces to improve separation resolution in protein analysis.[8,10-12] With silica-based nanosieves, the goal is to passivate free silanol groups to produce a mildly hydrophilic protein-repellent surface. Generally, there are two ways to chemically deactivate a surface: permanent modification and dynamic modification. Permanent modification utilizes covalent bonding and crosslinking of high molecular weight polymers. Dynamic modification uses small molecules, surfactants or polymers as buffer additives to generate non-covalently attached surface coatings. Permanent modification is more stable and effective than dynamic modification. However, it typically involves a lengthy synthesis process and viscous polymer solutions, which are hard to introduce into nanochannels and can easily cause clogging. Therefore, a dynamic coating, which can be prepared by simply rinsing a surface with a solution containing a coating agent, is more attractive for nanochannel deactivation.

Various polymeric buffer additives have been used in dynamic modification, such as polyoxyethylene (Brij-35), hydroxyethylcellulose (HEC), poly(ethyleneimine) (PEI), poly(vinyl alcohol) (PVA), poly(ethylene oxide) (PEO) and poly(vinylpyyrolidone) (PVP). Neutral polymers are more often used than charged polymers, as they eliminate electrostatic interactions between proteins and surfaces. The hydrophilicity of the coating polymer is very important. Increasing the hydrophilicity will reduce protein-surface interaction; however, it will also lower the stability of the absorbed coating.[13] I have experimented with the above-mentioned polymers, small amines and low-molecular-weight surfactants. Only PEO was shown to be protein-resistant

to some degree; however, it did not completely prevent protein adsorption on the nanochannel surface. A wide range of molecular weights (i.e. 400, 1000, 3350, 35 k, 100 k and 600 k) and different concentrations (5–20% for 400, 1000, 3350 and 0.05–2% 35 k, 100 k and 600 k) were evaluated. By far, PEO with the highest molecular weight (i.e. 600 k) was shown to be the most efficient in reducing protein adsorption.

As seen in **Fig. 2.7**, a set of 160-30 nm channels was tested for LDL trapping. LDL was labeled with fluorescent dye, AF 488, for detection. On bare silica walls, the proteins appeared to stick, and no trapping was obtained. When the channels were coated with 0.2% (w/v) PEO-600 k solution, surface adsorption was greatly decreased, and the proteins passed the barrier and stopped at the exit. Interestingly, when a higher concentration (0.4 %) of the PEO-600 k coating solution was applied, separation of the sample occurred. Part of the sample was trapped at the barrier while the rest migrated to the channel end. It is possible that the thicker polymer coating reduced the barrier height and produced an effective pore size smaller than 30 nm, which resulted in trapping of the LDL particles. Right now, I don't have a method to examine the inner surface of the channels. It would be useful to study the surface chemistry of the coated channel and determine whether or not and to what degree, the dimensions are changed by the polymer coating. De Gennes and co-workers reported the first theoretical studies of the resistance of PEO polymers to protein adsorption.[14] They concluded that a polymer brush, i.e. a layer of end-tethered PEO chains, served as a physical barrier. The steric repulsion resulting from compression of the PEO chains as the protein approached the surface was responsible for reducing protein adsorption. It was predicted that longer chain lengths and higher chain densities would lead to better protein resistance. Later, Szleifer et al. suggested that the mechanism for prevention of protein adsorption was simply blocking of protein adsorption sites (**Fig. 2.8**).[15-17]

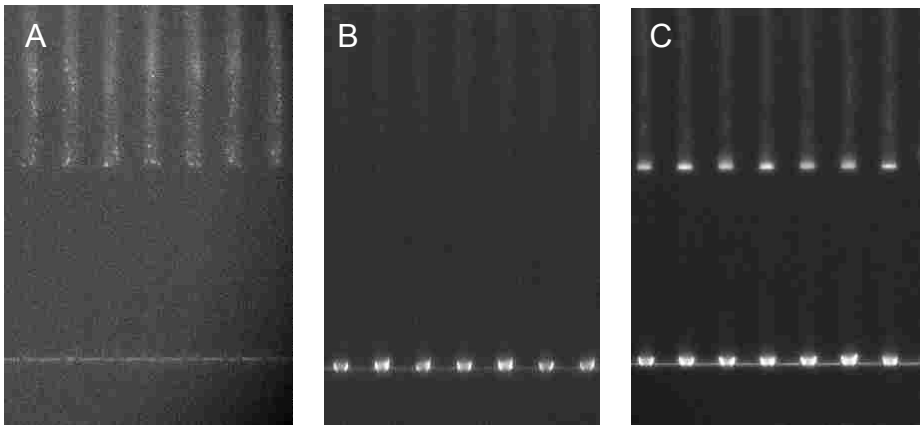

Figure 2.7 Fluorescence micrographs of AF488 labeled LDL (18–25 nm in diameter) in 160-30 nm channels. (A) When no surface coating is applied, proteins absorb onto the surfaces of the tall channel segments. (B) When the channels are pretreated with 0.2% (w/v) PEO-600 k solution, proteins pass the 30-nm barrier and accumulate at the channel exit. (C) When the channels are coated with 0.4 % (w/v) PEO-600 k, proteins are fractioned into two groups, one stopping at the barrier and the other at the channel end.

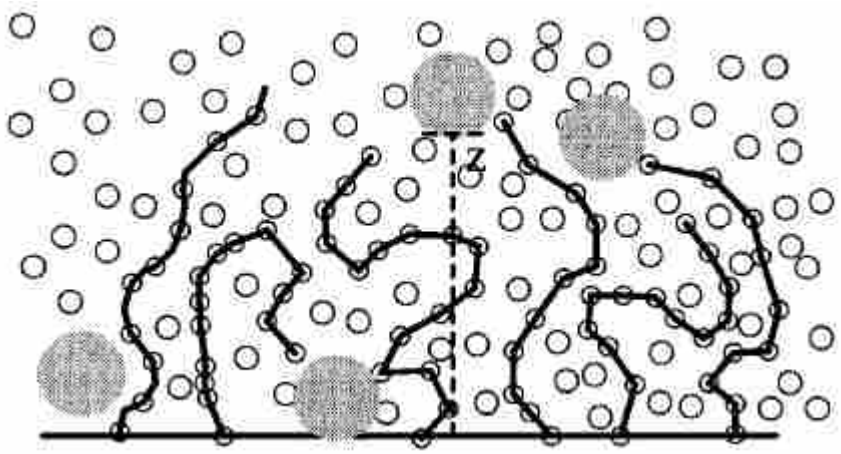

Figure 2.8 Schematic illustration of a grafted polymer layer in contact with a protein solution. The connected circles represent the polymer chains, the small circles are the solvent molecules and the large circles are the protein molecules (adapted from Ref. 15, with permission from Elsevier).

Although understanding the nonfouling mechanism of PEO is still ongoing, a possible explanation for the deactivation efficiency of PEO-600 k is that it possesses the longest chain among all of the PEOs evaluated. Longer chain length results in larger excluded volumes, higher conformation entropy and more pronounced steric repulsion. Concentrations higher than 0.2 % were tested, but showed inferior protein resistance. Higher concentrations should result in higher chain densities, which is typically desirable because this makes it more difficult for proteins to diffuse to the underlying substrate. However, if the density is too high, the chains may dehydrate and become adsorbent for proteins. For instance, worse adsorption was observed in the 160-nm segments when a 0.4 % instead of 0.2 % coating was used. In dynamic modification, PEO attaches to the silanol groups via hydrogen bonding. Silanol groups must be fully protonated to achieve good coating characteristics, so rinsing the surface with hydrochloric acid before PEO solution is necessary.

2.4.2 Separation of binary protein mixtures and dual-color fluorescence detection

It is a common procedure to use thyroglobulin (17.0 nm), apoferritin (12.2 nm), catalase (9.6 nm), lactate dehydrogenase (8.2 nm) and BSA (7.1 nm) as calibration proteins in gel electrophoresis for lipoprotein analysis, due to their size similarities to HDL and LDL. I first studied the separation of these standards before lipoproteins, which have more complex compositions and structures. In this section, separation of a binary protein mixture of BSA and thyroglobulin (TG) was demonstrated in 160-25 nm channel array. Dual color detection was accomplished by labeling BSA with a green dye, fluorescein isothiocyanate (FITC, excitation/emission, 490 nm/525 nm) and TG with a red dye, Alexa Fluor 647 (AF 647, excitation/emission, 650 nm/665 nm). Static fluorescence images were obtained with an upright microscope. A blue LED (470 nm) or a red LED (660 nm) was used for excitation of FITC or AF

647, and a CCD camera was used for detection. A FITC filter cube (BP 485/20 nm excitation filter, LP 515 nm emission filter) was used to image FITC-BSA, and a Cy5 filter cube (BP 630/20 nm excitation filter, BP 667/30 nm emission filter) was used to image AF 647-TG.

The hydrodynamic diameter is approximately 7.1 nm for BSA and 17.0 nm for TG. **Fig. 2.9** shows that when 0.5 mg/mL BSA and 0.5 mg/mL TG were injected into the channels separately, TG was trapped at the barrier while BSA was collected at the channel exit. When a 1:1 mixture of the two protein samples was introduced into the channels, separation was observed, showing one fraction stopping at the barrier and the other at the end (proteins accumulated at the exit could only be BSA). The fluorescent signal at the barrier for the mixture was more intense than that for TG alone and the signal at the end was weaker than that for BSA alone. These results suggest that some BSA was also trapped, mostly likely due to blockage by the TG particles that arrived at the barrier first. An alternating AC field was effective in reducing channel clogging in separations of polymer beads and viruses. However, this method was not successful when applied to proteins due to non-specific adsorption. I will discuss the AC agitation method in detail in the next Chapter.

These preliminary results demonstrate the potential of using nanosieves for separating protein mixtures. However, three major issues must be addressed: (a) nonspecific adsorption, (b) clogging and (c) presence of an energy barrier at the channel interface, which requires passivation of the inner channel wall and application of an electric field along the channel length to provide a driving force after capillary action ceases.

Interestingly, LDL particles with diameter of 18–25 nm passed the 30 nm barrier with no retention (**Fig. 2.7**). However, polymer beads and other types of proteins (e.g., 17 nm TG trapped at 25 nm interfaces) were not able to pass a barrier larger or equal to their size due to the

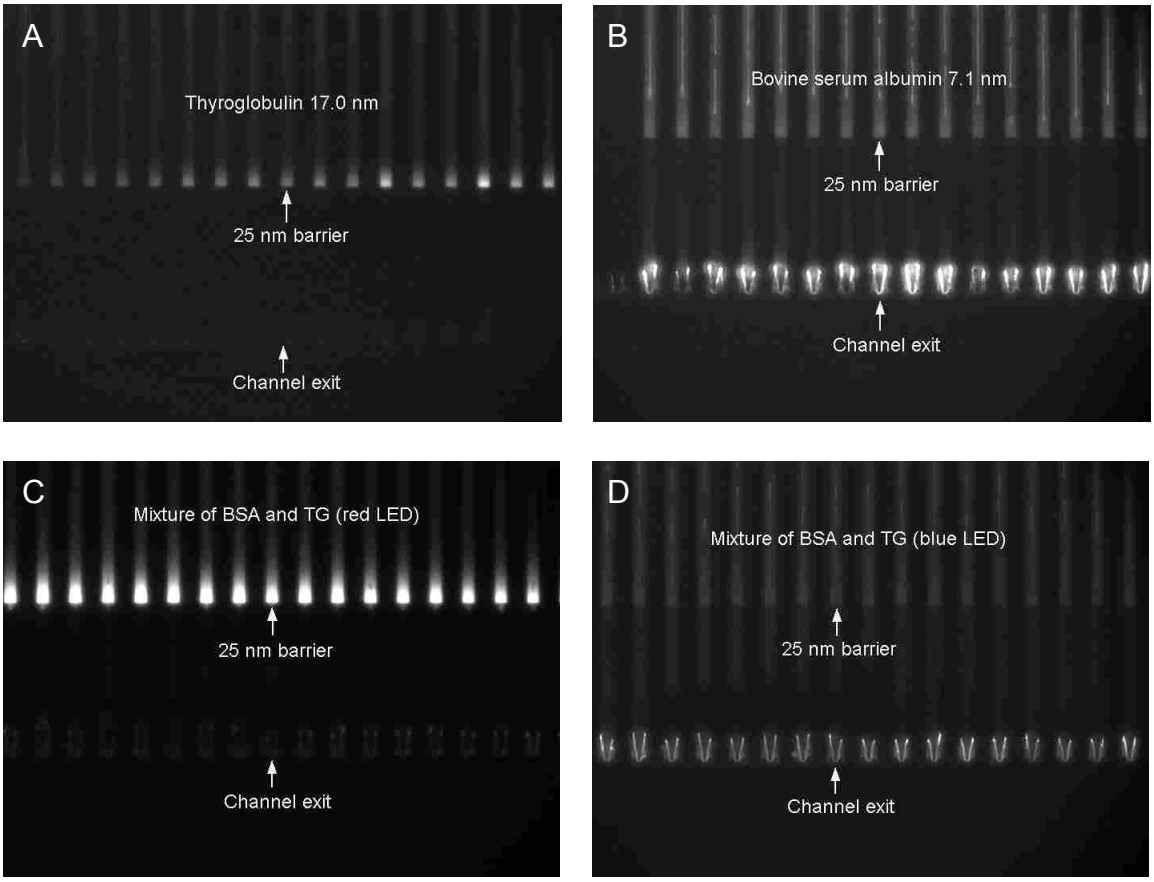

Figure 2.9 Micrographs showing trapping of BSA and TG and separation of their mixtures in 160-25 nm channels. (A) 0.5 mg/mL TG stopped at 25 nm barrier. (B) 0.5 mg/mL BSA passed the barrier and accumulated at the channel end. (C) and (D) Same trapping experiments imaged with different filter sets and illumination sources; (C) AF647 filter and red LED, and (D) FITC filter and blue LED.

existence of an energy barrier. It is unclear as to what caused LDL to behave differently in this situation. A possible explanation is that Giddings' model applies to rigid particles, while proteins are flexible and can undergo conformational changes, especially when subject to interactions with solid surfaces. Mikl et al.[18] studied lipoprotein resilience using elastic incoherent neutron scattering (EINS), which is a well-suited method to investigate the overall dynamics of complex biological systems like cells, membranes or lipoprotein, and revealed that lipoproteins are extremely soft and flexible. Also, it is known that circulating VLDL can undergo metabolic delipidation to form IDL and LDL of smaller sizes.[19] It has been reported that artificially-prepared lipid-containing vesicle liposomes also lose lipids when experiencing frictional forces.[20] Therefore, delipidation may occur in nanochannels due to protein-surface interactions, which reduce the sizes of lipoproteins. Additional studies must be done to determine the reasons behind the differences observed in trapping behavior between rigid and flexible particles, and between lipoproteins and other types of proteins.

2.5 References

1. Arduino, P.G.; Porter, S.R. *J. Oral. Pathol. Med.* **2008**, *37*, 107-121.
2. Patient, R.; Hourioux, C.; Sizaret, P-Y; Trassard, S.; Sureau, C.; Roingeard, P. *J. Virol.* **2007**, *81,* 3842-3851.
3. Ishihama, Y.; Rappsilber, J.; Andersen, J. S.; Mann, M. *J. Chromatogr., A* **2002**, *979*, 233-239.
4. Kennedy, R. T.; Jorgenson, J. W. *Anal. Chem.* **1989**, *61*, 1128-1135.
5. Lord, G. A.; Gordon, D. B.; Myers, P.; King, B. W. *J. Chromatogr., A* **1997**, *768*, 9-16.
6. Giddings, J. C.; Kucera, E.; Russel, C. P.; Myers, M. N. *J. Phys. Chem.* **1968**, *72*, 4397-4408.

7. Leckband, D. *Annu. Rev. Biophys. Struct.* **2000**, *29*, 1-26.

8. Liu, J. K.; Lee, M. L. *Electrophoresis* **2006**, *27*, 3533-3546.

9. Nakanishi, K.; Sakiyama, T.; Imamura, K. *J. Biosci. Bioeng.* **2001**, *91*, 233-244.

10. Ishihara, K.; Nomura, H.; Mihara, T.; Kurita, K.; Iwasaki, Y.; Nakabayashi, N. *J. Biomed. Mater. Res.* **1998**, *39*, 323-330.

11. Wendorf, J. R.; Radke, C. J.; Blanch, H. W. *Biotechnol. Bioeng.* **2004**, *87*, 565-573.

12. Evers, F.; Steitz, R.; Tolan, M.; Czeslik, C. *Langmuir* **2011**, *27*, 6995-7001.

13. Horvath, J.; Dolnik, V. *Electrophoresis* **2001**, 22, 644-655.

14. Jeon, S. I.; Lee, J. H.; Andrade, J. D.; De Gennes, P. G. *J. Colloid Interface Sci.* **1991**, 142, 149-158.

15. Szleifer, I. *Biophys. J.* **1997**, *72*, 595-612.

16. Mcpherson, T.; Kidane, A. Szleifer, I.; Park, K. *Langmuir* **1998**, *14*, 176-186.

17. Fang, F.; Szleifer I. *Proc. Natl. Acad. Sci.* **2006**, *103*, 5769-5774.

18. Mikl, C.; Peters, J.; Trapp, M.; Kornmueller, K.; Schneider, W. J.; Prassi, R. *J. Am. Chem. Soc.* **2011**, *133*, 13213-13215.

19. Berneis, K. K.; Krauss, R. M. *J. Lipid Res.* **2002**, *43*, 1363-1379.

20. Krafft, M. P.; Riess, J. G. *Chem. Rev.* **2009**, *109*, 1714-1792.

Chapter 3. Three-segment nanochannels

3.1 Introduction

Two-segment nanochannels are the simplest configurations of the nanosieve arrays, and they have provided fundamental understanding of how trapping and separation occur in this type of geometry. However, due to the existence of energy barriers, it was unclear using these two-segment arrays alone whether or not particle mixtures could be fractioned using capillary action only and whether or not the obtained data could be interpreted as true size distribution information. Furthermore, with channels having only two different heights, no more than two size fractions could be obtained. More detailed size profiling would require adding multiple height variations to the nanochannel structures. As the first step toward this, I constructed three-segment nanochannels containing two height barriers. As expected, an equilibrium distribution also exists in three-segment channels and an external field was required to help the particles overcome the configurational entropic energy barrier and to eliminate potential channel clogging. I investigated the effects of surfactants and an applied oscillating electric field. Different particle sizes, such as 30 nm, 50 nm, 80-100 nm and 120 nm polymer beads were used and different channel dimensions were fabricated. Only trapping of 30 nm particles (polymer beads and HBV virus capsids) will be described in this dissertation. Devices with heights stepping from 208 nm to 54 nm, then further down to 30 nm were fabricated and used to investigate the trapping behavior of these particles, which actually ranged in size from 30 to 50 nm. The questions of interest included: Would all particles stop at the 30 nm interfaces? What would the distribution ratio be between particles trapped at the two interfaces? Would the same-size polymer beads and virus particles display different trapping behaviors?

3.2 Fabrication

The three-segment channels consisted of 208 nm, 54 nm, and 30 nm high segments connected in series (0.8 mm, 0.2 mm and 0.2 mm long, respectively). Similar to the fabrication process for two-segment channels, the preparation of three-segment chips began with depositing approximately 200 nm of silicon dioxide on a silicon substrate via PECVD. A 30 nm layer of aluminum was then deposited using a thermal evaporator to form the short segments. Photoresist AZ nLOF 2020 was spun on, patterned and developed, exposing an area where a second layer of aluminum was deposited to form the 54 nm tall segments. The photoresist was then lifted off using N-methylpyrrolidone (NMP) heated to 95˚C, leaving two aluminum covered areas of different heights. The photolithography step using AZ nLOF 2020, metal deposition and NMP lift-off was then repeated, defining three distinct segment heights of 30 to 54 to 208 nm. After that, AZ 3330 PR was spun on and patterned to define the aluminum core lines. The exposed aluminum was removed using a commercial aluminum etchant heated to 50˚C, and the photoresist was rinsed off with acetone and 2-propanol. The aluminum channel core heights were verified with atomic force microscopy (AFM). Then, a capping layer of approximately 5 μm silicon dioxide was deposited using PECVD. The reservoir regions were then patterned on the wafer via photolithography using AZ 3330 and removed using buffered oxide etchant (BOE). The sacrificial cores were etched by soaking the wafer in aqua regia (HNO_3/HCl, 1:1) and then in Nanostrip, both at 130˚C overnight. The final step involved soaking the wafer in DI water overnight to ensure neutral pH inside the channels.

3.3 Device operation

To introduce sample into the nanochannel array, a pair of rectangular reservoirs (8 mm long × 0.6 mm wide × 0.5 mm deep) was laser cut into a piece of 0.5 mm thick, 10 mm × 10 mm acrylic plate and treated on both sides with an oxygen plasma for 30 s at 150 W. A clean Si wafer was partially spin-coated with NOA 76 epoxy solution (Norland Products, Cranbury, NJ) at 5000 rpm for 1 min, onto which the PMMA reservoirs were pressed lightly to pick up a uniform coating of epoxy. Then the reservoirs were pressed onto the chips using tweezers, making certain that the on-chip reservoirs were not covered, and the channel inlets and outlets were open to allow sample introduction and evaporation, respectively. The assembly was then placed under a UV light for approximately 20 min and further cured in an oven overnight at 50˚C.

Chromeon 470 labeled, carboxy-modified 30 nm polyacrylonitrile nanobeads (Sigma Aldrich, St. Louis, MO) were first used as analytes. The original bead concentration was approximately 3×10^{14} particles/mL, which was diluted by a factor of either 10 or 50 using 100 mM Tris-HCl (pH 8.3) containing 1 mM SDS (Columbus Chemical Industries, Columbus, WI). HBV capsids were obtained from the laboratory of A. Zlotnick and were labeled with Alexa Fluor 488 and purified using 30 kDa membrane filters (Amicon Ultra-0.5, Millipore, Billerica, MA). Specifically, a 500 µL volume of the virus sample was added to the filter, which was placed in a microcentrifuge tube and spun twice at 13,000 rpm for 7 min each. Between the two spinnings, filtrate was discarded and sample was brought to 500 µL again with 100 mM Tris buffer containing 1 mM SDS. To recover the concentrated sample, the filter device was placed upside down in a clean microcentrifuge tube and spun at 3,500 rpm for 2 min.

Trapping was monitored using a CCD camera (CoolSNAP HQ2, Photometrics, Tucson, AZ) attached to an upright microscope (Axio Scope A1, ZEISS, Thornwood, NY). Illumination was provided by a 625 mW LED (MBLED, Thorlabs, Newton, NJ) that passed through a filter cube (FITC-LP01-Clinical-OMF, Semrock, Rochester, NY). Images were acquired sequentially at a rate of 1.33 frames per second. Trapping was quantified by measuring the changes in fluorescence signal intensity for particles accumulated at the barriers or the ends of the multiple nanochannels over the whole trapping period. Image acquisition and data analysis were performed using Image J software. All trapping data were normalized to the maximum fluorescence intensity.

For AC electrophoretic experiments, platinum wires were placed in the inlet and outlet fluid reservoirs, and an AC function generator (Hewlett Packard HD 3312 A, Palo Alto, CA) and an oscilloscope (TDS3014 4Ch 100MHz, Tektronix, Beaverton, Oregon) were used to control and monitor the AC frequency, waveforms and DC offset applied to the devices.

3.4 Attachment of poly(methyl methacrylate) reservoirs

Many lab-on-a-chip devices utilize a micro reservoir for direct chemical analysis or for fluid introduction into the channel system.[1-4] I developed a reservoir that allowed me to interface nanochannels with microliter-scale fluid volumes. As described in the experimental section, the nanochannels were made from SiO_2. However, the reservoir regions were etched down to the underlying Si. Since both Si and SiO_2 surfaces are hydrophilic, liquid samples could flow through the nanochannels smoothly via capillary action. However, due to the extremely small inner volume of the nanochannels (pL) and the limited depth of the on-chip liquid reservoir (5 μm), liquid samples oftentimes tended to wick along the outer surface over the channels, instead

of flowing into and through the nanochannels or remaining in the reservoirs. The situation became worse when surfactants were used because they reduced the surface tension of the solution, which helped to spread it across the surface. To solve this problem, I constructed PMMA reservoirs via laser-cutting and attached them to the nanofluidic chips by epoxy resin bonding (**Fig. 3.1**).

To produce a good reservoir that prevented clogging and leakage, it was essential to use a thin, clean PMMA plate to achieve high-quality contact and good sealing between the reservoir and the chip. I found that 0.5 mm was the best thickness of PMMA to use. Second, alignment precision must be achieved using a tunable stage with fine xyz control, because if misalignment occurred, the uncured resin would wick into the nanochannels through capillary action and clog them. For the same reason, a well-controlled epoxy layer thickness was also important, and I found that spin coating at 5000 rpm for 1 min gave the best results. Construction of these PMMA reservoirs was relatively simple and fast, and yielded an 81% success rate (65 out of 80 reservoir-attached chips). Testing of the reservoirs affixed to the chips proved that they held the liquid samples without leakage even after months of use.


A

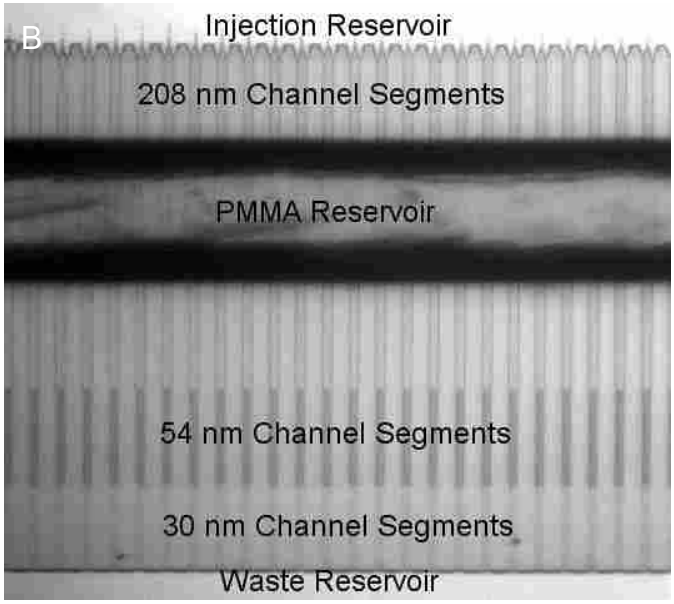
B
Injection Reservoir
208 nm Channel Segments
PMMA Reservoir
54 nm Channel Segments
30 nm Channel Segments
Waste Reservoir

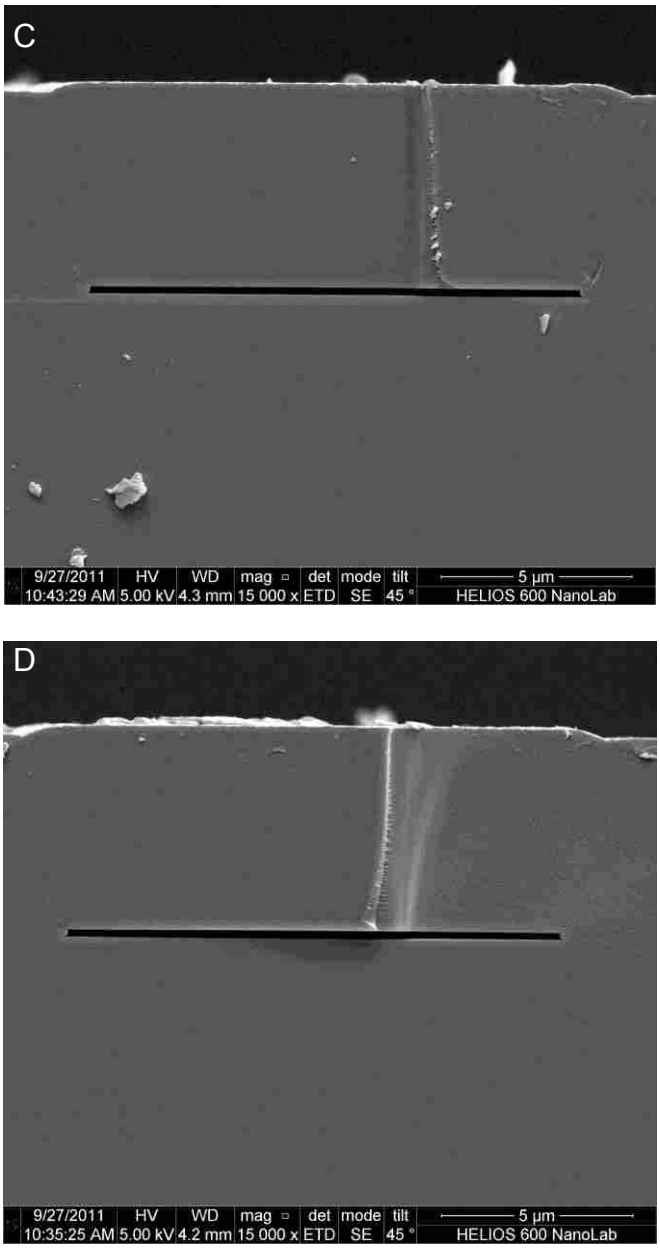

Figure 3.1 (A) Photograph of a 208-54-30 nm three-segment chip with an attached PMMA reservoir set next to a US quarter coin; (B) microscope view of the three-segment nanochannels in (A), with the 208 nm tall segments partially covered by the PMMA reservoir and the 54 nm and 30 nm interfaces uncovered for convenience of imaging; (C and D) SEM images of the cross-sections of two different 208 nm segments in a 208-54-30 nm nanofluidic device, demonstrating the uniformity of the channels.

3.5 Size fractionation of polymer beads

Using two-segment (200-45 nm) chips, partial trapping at the interface was observed for the 30 nm particles. Because silanol groups on the inner nanochannel surface display a negative charge at alkaline pH conditions, to prevent nonspecific adsorption and unwanted aggregation of the particles, I used negatively charged SDS as a buffer additive. The surfactant was expected to adsorb on the particle surface, imparting a negative charge to the particles, repelling them from the channel walls and increasing their colloidal stability.[5] The critical micelle concentration (CMC) of SDS has been reported to be around 7–10 mM in water at 20-25˚C and, in order to avoid forming SDS micelles, only concentrations below 7 mM were used. The aggregation number and micellar diameter at the CMC are approximately 62 and 6 nm, respectively.[6]

The distinct difference in trapping results obtained with and without added SDS proved the necessity of using a surfactant. In **Fig. 3.2A**, no SDS was used and all 30 nm particles were retained at the 54 nm barrier. Adsorption along the channel walls can also be observed. When 1 mM SDS (**Fig. 3.2B**) was added to the buffer, particles became distributed between the 54 nm barrier and the 30 nm barrier at a ratio of approximately 1.5:1 (**Fig. 3.2C**).

To study the effect of SDS concentration, a series of concentrations (1, 2, 4 and 6 mM) was investigated. It was found that, at a concentration higher than 4 mM, clumps of fluorescent beads appeared, which were slowly dragged along the channel walls. Since SDS is concentrated due to evaporation from the channel ends and in the reservoir, there is a chance that its actual concentration is higher inside the nanochannels than in the original sample, approaching the CMC of SDS. I deduced that at concentrations above 4 mM, aggregation of SDS began, which caused aggregation of particles. Most likely, the SDS micelles (6 nm) attached to the polymer beads, resulting in sizes larger than 30 nm.

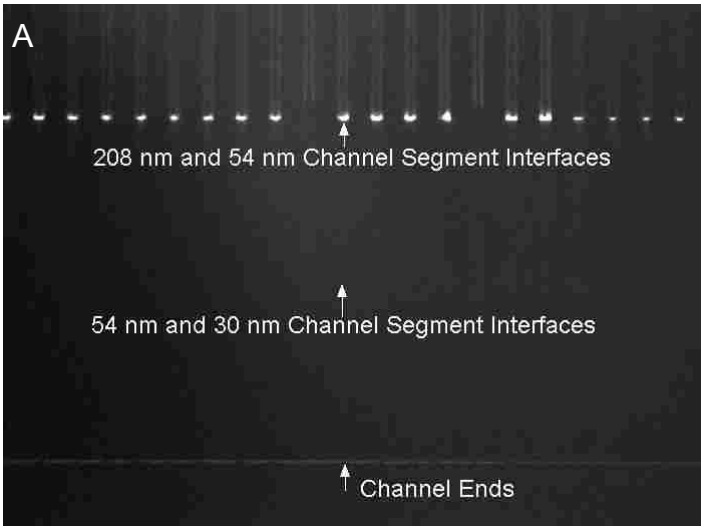
A
208 nm and 54 nm Channel Segment Interfaces
54 nm and 30 nm Channel Segment Interfaces
Channel Ends

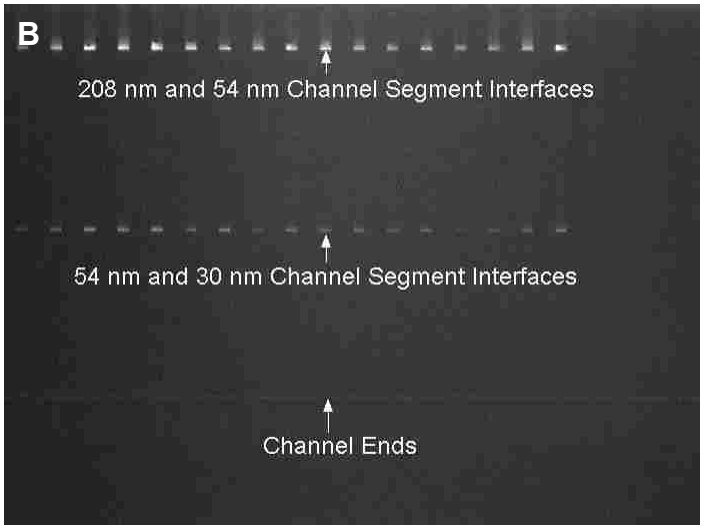
B
208 nm and 54 nm Channel Segment Interfaces
54 nm and 30 nm Channel Segment Interfaces
Channel Ends

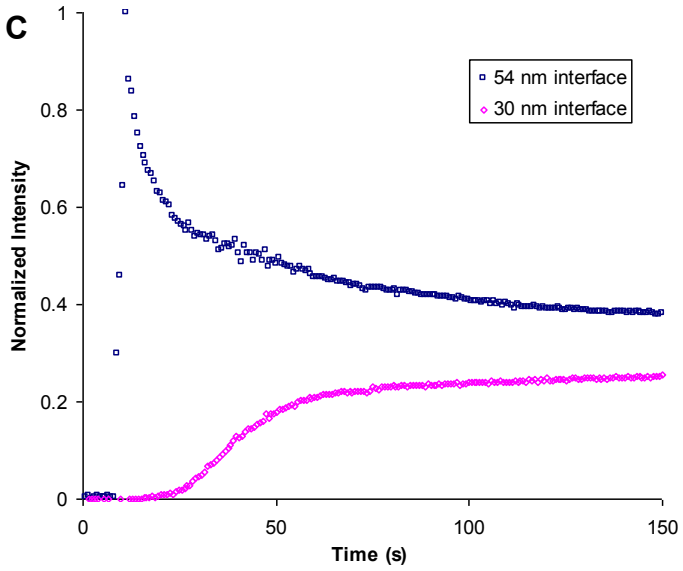

Figure 3.2 Capillary action based separations of 30 nm particles (3×10^{13} particles/mL) in 208-54-30 nm channels. (A) No SDS added; all beads were stopped at the 54 nm barrier and adsorption along the 208 nm tall segment channel walls was observed; (B) 1 mM SDS was added in the buffer, and some particles passed through to the 54 nm interfaces; (C) normalized fluorescence signal intensity versus time indicating that, in (B), the particles separated at the 54 nm interfaces and the 30 nm interfaces with a ratio of 1.5:1.

I compared particle trapping results for approximately 20 individual channels on each of six different chips with SDS concentrations ranging from 1 to 4 mM; 4 to 5 trappings were performed on each chip. Using 1 mM SDS, average distribution ratios of particles trapped at the 208-54 nm interface to those trapped at the 54-30 nm interface ranged from 1 to 3 (**Table 3.1**). Since using higher concentrations did not improve the distribution of particles significantly (2:1 for 2 mM and 4:1 for 4 mM), in order to minimize the chance of forming SDS micelles, a concentration of 1 mM SDS was used for all trapping experiments with polymer beads.

Based on the model trapped/total = d_p/h, a smaller fraction of 30 nm diameter particles should stop at the larger 54 nm barrier of the three-segment chips compared to the 45 nm barrier of the two-segment chips (see section 2.3). However, the above results showed that 50% of the particles stopped at the 45 nm height step, whereas 66% were stopped at the 54 nm height step. I hypothesize that the channels became clogged, which could be caused by several factors. First, unlike circular channels, rectangular nanochannels exhibit a flow stagnation phenomenon in the sharp corners (especially at the interfaces) due to the symmetric velocity profile,[7] which tends to retain particles. With the particle size being so similar to the channel height, particles can quickly build up and constrict the pathway. Second, in order to pass through the interfaces, particles must overcome the configurational entropic energy barrier. This can also slow down capillary-induced flow, and stack particles at the barriers. The 208-54-30 nm channels are more likely to be jammed or clogged than the 200-45 nm channels since they have one more interface and the smaller height slows down capillary flow.

I compared trapping experiments using two- and three-segment channels in order to further understand the fluidic motion and molecular motion inside different nanochannel structures. By referring to the resultant trapping intensity graphs, it is easy to notice a unique

Table 3.1 Consistency in particle distribution ratios between different channels on different chips for capillary action-based separations of 30 nm particles (3×10^{13} particles/mL) in 208-54-30 nm channels for various SDS concentrations.

SDS Conc. (mM)	Chip	Particle Distribution Ratio (54 nm/30 nm Barrier)	Particles Loaded per Channel ($\times10^4$)		Relative Std. Dev. (%)	
			54 nm Barrier	30 nm Barrier	Intra-chip	Inter-chip
1	a	3.0	4.5	1.5	6.7	0.07
	b	2.8	4.4	1.6	10.6	
2	c	2.3	4.2	1.8	10.0	0.08
	d	2.4	4.2	1.8	13.4	
4	e	3.0	4.5	1.5	9.8	3.8
	f	4.3	4.9	1.1	5.0	

difference in the two types of channel structures. In the 200-45 nm channels (**Fig. 2.5B**), trapping at the interfaces and at the ends appeared to start almost simultaneously, and the signal intensities reached a maximum and stabilized in approximately 30 s. The intensity built up faster at the interfaces than at the ends, which was reasonable considering the flow direction. For the 208-54-30 nm channels (**Fig. 3.2C**) the fluorescence intensities at the 54 nm interfaces reached a peak and then decreased before stabilizing, indicating that some particles were temporarily trapped, but eventually passed through the interfaces. This was also reflected in the curve corresponding to trapping at the 30 nm interfaces, where I observed a lag in the onset of trapping. However, considering the fact that the tall and short interfaces were merely ~ 200 μm apart, trapping would be expected to begin almost simultaneously at the two interfaces as in the two-segment chips. Again, it seemed that, regardless of size, all particles lingered at the tall interfaces before some passed through. A particle "dam" may have formed at the tall interfaces as capillary-driven flow tried to carry the small particles toward the end. Once capillary action was completed, no other force present was strong enough to help the smaller beads overcome the energy barrier and pull them through the first interface as they arrived from the inlet and accumulated at the interface, which further restricted passage. Two observations are related to this postulate. First, as mentioned earlier, in the 208-54-30 nm chips, an average of 66% of the 30 nm particles accumulated at the 54 nm barrier, even though they were predicted to accumulate at the 30 nm barrier. Second, the line plots showed that the fluorescence intensity stabilized in ~30 s for the 200-45 nm channels and in ~80 s for the 208-54-30 nm channels. Since completion of trapping can be related to stability of the fluorescence signal, the conclusion was reached that it takes more than twice the time to trap using a three-segment channel compared to a two-segment channel.

3.6 AC electrophoretic agitation

It has been demonstrated that the application of an electric field can pull charged particles into the pores, which helps overcome the energy barrier.[8] Therefore, to eliminate clogging and ensure that trapping of the nanoparticles was solely based on size and not a result of other factors, an oscillating potential was applied to drive the particles forward and backward in an effort to break aggregates into individual particles and allow them to flow through the channels.

The dielectric breakdown mechanism of silicon dioxide specifies that when the local electric field is sufficiently high, breakdown of the dielectric SiO_2 layer occurs and causes a short circuit. For ~250 nm thick SiO_2, the critical breakdown voltage is 7 to 10 V.[9] Consequently, to avoid shorting through the bottom silicon dioxide layer on the nanochannels, I only used low voltages (lower than 10 V). The polyacrylonitrile-based 30 nm nanobeads were negatively charged due to the surface carboxyl groups and the adsorbed SDS molecules, and they responded to electrokinetic migration when subjected to the electric field. Electrokinetic migration included both electrophoresis and electroosmosis, which were in opposite directions for negatively charged analytes. In a typical microchannel, the Debye layer thickness is negligible compared to the dimensions, whereas in a planar nanochannel, the Debye length (λ_d) becomes comparable to the channel depth. Using the equation

$$\lambda_d(nm) \approx 9.6/(c^{1/2}z) \tag{3.1}$$

where c is the solution concentration in mM and z is the valency,[10] the thickness ranges from 1 to 200 nm for a monovalent electrolyte in a concentration ranging from 0.002 to 100 mM, indicating possible overlap of the electrical double layer at low ionic strengths, which leads to uneven electroosmotic forces inside the channels. In order to maintain uniform electroosmotic

flow inside the nanochannels, I used a high ionic strength buffer (100 mM), which gave a 1-nm Debye layer, which was small compared to the channel depth.

AC or DC voltages were applied by placing a grounded electrode in the injection reservoir and a positively biased electrode in the outlet reservoir so that capillary flow and electrophoretic migration would be in the same direction. In the case of DC, the voltage was varied between 1 and 10 V, and no particles were observed to move from the tall interfaces to the short ones. By varying the peak value of the sinusoidal (symmetrical) AC field from 1 to 8 V, DC offset between 1 and 8 V, and frequency from 50 to 1000 Hz, it was determined that significant particle redistribution happened when applying a sinusoidal wave with a frequency of 150 Hz and a peak-to-peak voltage of 8 V (4 V DC offset). Under these conditions, many particles trapped at the 54 nm interfaces moved down to the 30 nm interfaces. Most interestingly, in some channels, no particles remained at the 54 nm interfaces, as they had all passed to the 30 nm interfaces (**Fig. 3.3A**). Based on the fact that an AC field was more effective than a DC field, it was concluded that the utilization of oscillating low-frequency AC waveforms alternated the direction of the electrophoretic force and, thus, particles moved in opposite directions every 0.0067 s. The agitation helped break up clumps (aggregates) into individual particles and redistribute them across the interfaces. When higher than 150 Hz frequencies were used, the particles did not have sufficient time to separate.

It was observed that the electric field strength (E) in the channels was inhomogeneous. As E is inversely proportional to the channel depth, the effective electric field strength was higher in the shallow segments compared to the deep segments. For example, for the 208-54-30 nm channels(the three segments were 0.8 mm, 0.2 mm and 0.2 mm long, respectively), the average height was approximately 153 nm and, thus, the field strength in the 30 nm channel

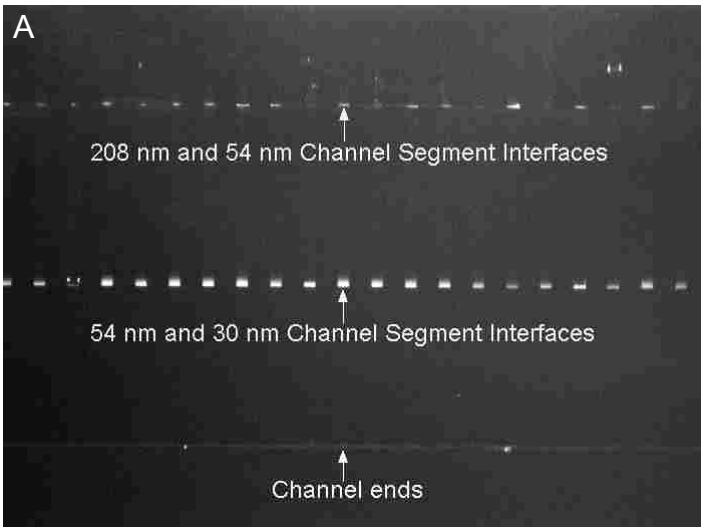
A
208 nm and 54 nm Channel Segment Interfaces
54 nm and 30 nm Channel Segment Interfaces
Channel ends

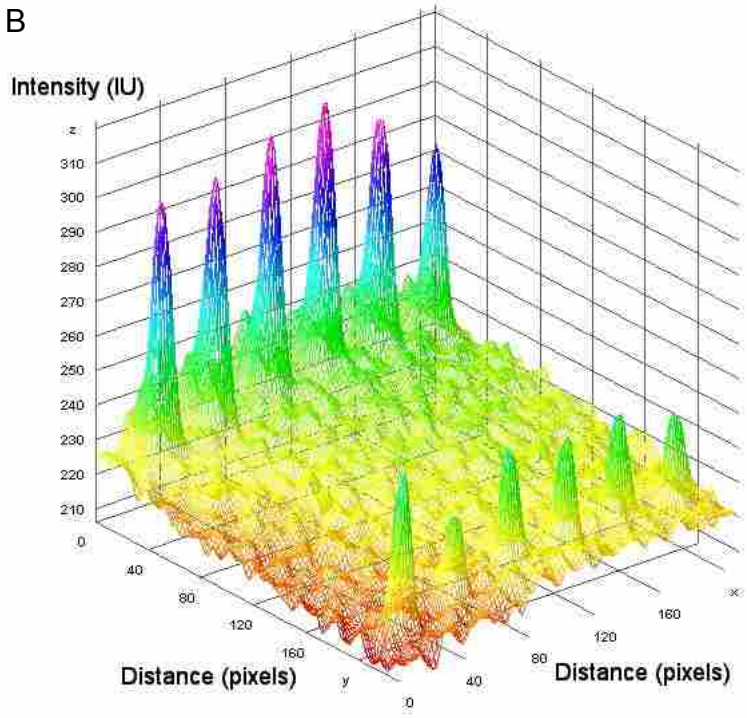
B
Intensity (IU)
z
310
300
290
280
270
260
250
240
230
220
210
0
40
80
120
160
Distance (pixels)
y
0
40
80
120
160
Distance (pixels)
x

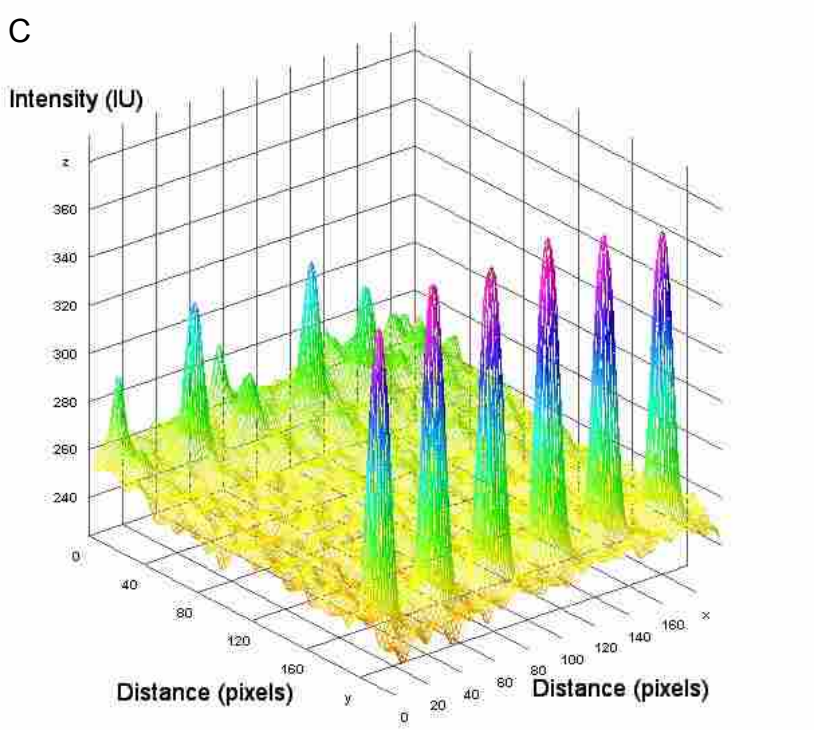

Figure 3.3 Images showing the effects of AC on eliminating clogging. (A) CCD image of trapped 30 nm polymer beads in 208-54-30 nm channels after being exposed to an oscillating electric field. (B) Three-dimensional image (xy distance vs. z fluorescence) demonstrating that, before an AC electric field was applied, most particles were stopped at the 54 nm interfaces; (C) three-dimensional image (xy distances vs. z fluorescence intensity) demonstrating that, after an AC electric field was applied, many particles migrated to the shorter 30 nm interfaces.

segments was a factor of 5 higher than the average field strength (~33 V/cm) when a 4 V DC offset was used. Although electroosmotic flow is essentially eliminated relative to electrophoretic motion of the particles in an AC field with no DC offset,[11] when there is a DC offset, there should be EOF. It was assumed that, by using a high ionic strength buffer, any electroosmotic flow was effectively quenched.[12] However, EOF was stronger in the shorter segments, where the field strength was higher. Stronger EOF led to competition with the electrophoretic migration by carrying particles in the opposite direction. Furthermore, the surface charge on the nanoparticles can vary from particle to particle, depending on the number of SDS molecules adsorbed onto them and the number of carboxyl groups on the surface. Also, some particle clumps may be easier to break up than others. In summary, these factors are most likely responsible for less trapping of particles in some channels at the 54 nm interfaces, whereas in other channels they were retained.

3.7 Trapping of hepatitis B virus particles

One issue associated with applying nanosieving to a biological sample mixture is the expected greater interactions of the biological particles with each other and with the channel walls via electrostatic and hydrophobic interactions, which lead to agglomeration and adsorption onto the walls. To test the ability of the three-segment chips to fractionate a biological sample, I attempted to trap pure HBV capsids with an average diameter of 30 nm. The similarity in diameter between the 30 nm polymer beads and the virus capsids allowed a direct comparison of trapping performance.

The initial trapping experiments in 208-54-30 nm channels showed that the viral particles separated into three fractions (**Fig. 3.4A**). Although both the viral particles and the polymer

nanobeads were spherically shaped, they were different in three aspects. First, the virus capsids were relatively uniform in size, whereas the polymer beads had a size distribution ranging from 30 to 50 nm. Second, the viral particles were sticky and were more prone to agglomerate and clog the channels compared to the polymer beads. Third, virus capsids are structurally more flexible than synthetic polymer beads and can undergo conformational deformation.

Based on these considerations, I deduced several reasons to explain why the 30 nm viral particles separated into three fractions and yet the same size polymer beads did not. Trapped bands formed at both the 54 nm and 30 nm interfaces, which were attributed to the existence of an entropic energy barrier and agglomeration as in the situation of polymer bead trapping. However, some of the viral particles and none of the polymer beads migrated to the ends of the channels, which suggests conformational flexibility of the viral particles. Even when an electric field was applied, the rigidity of the polymer beads prevented them from passing into the 30 nm segments.

When an AC electric field was applied to the trapped sample (7 V DC offset and 200 Hz), all viral particles were transported to the ends of the 30 nm short segments (**Fig. 3.4B**). Because the negatively charged viruses are likely more pliable than the rigid polymer beads, the applied AC field not only helped the capsids overcome the barrier to entering the short segments, but also broke up the agglomerated particles. Meanwhile, with the viruses moving all the way to the ends of the 30 nm segments, it was suspected, similar to a tennis ball being squeezed, that the electric field caused the viruses to distort slightly as they passed through the short segments.

These results demonstrate that AC electrophoresis is an effective way to eliminate particle agglomeration. Thus, trapping can be based principally on size without being influenced by aggregation, channel clogging and energy barriers.

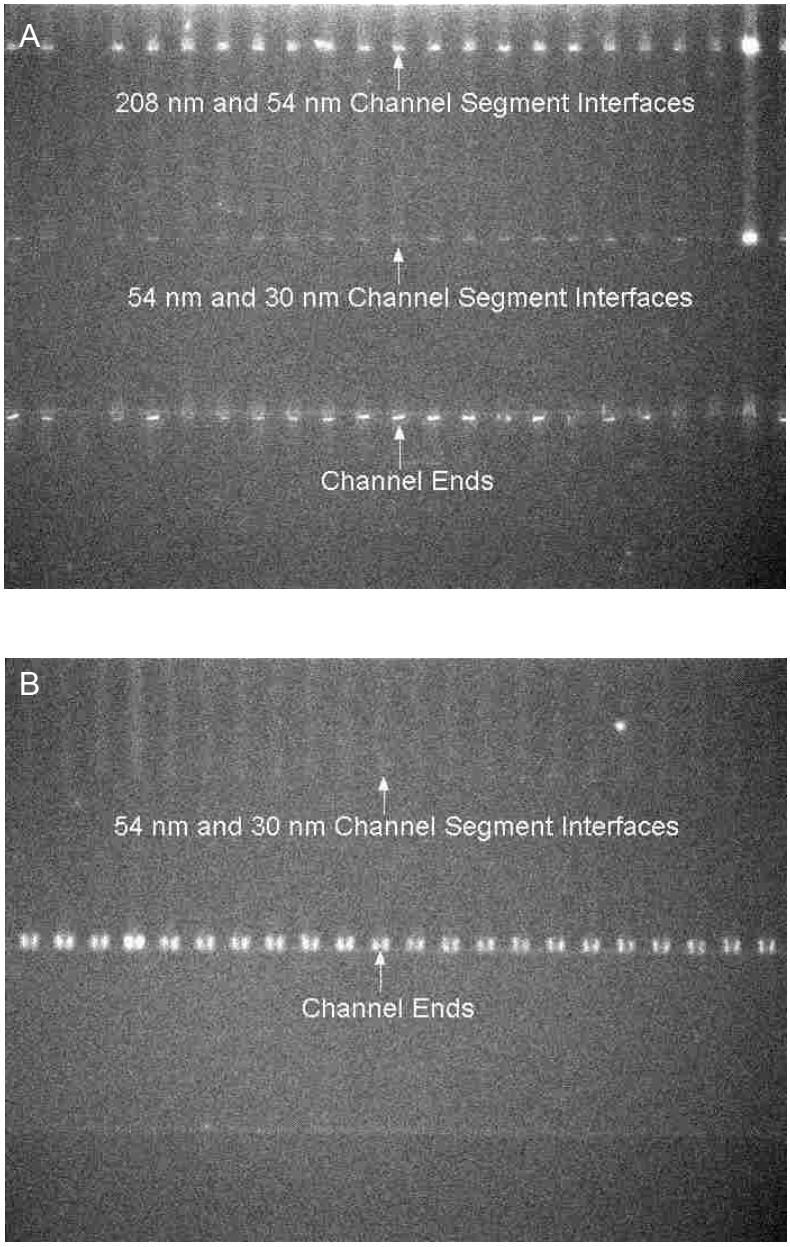

Figure 3.4 Trapping of 30 nm HBV capsids in 208-54-30 nm channels. (A) CCD image showing capillary action-based separations of the viral particles; (B) CCD image showing redistributed viral capsids after being exposed to AC (200 Hz and 7 V DC offset), in which all particles were transported to the ends of the 30 nm short segments.

3.8 Lipoproteins

3.8.1 Trapping of human plasma lipoproteins

As mentioned earlier, this work was originally directed toward size-based separation of lipoprotein mixtures. In previous experiments on protein trapping, it was discovered that lipoproteins pass barrier heights equivalent to their diameter. Corresponding to the diameters of different lipoprotein classes (VLDL, 30-80 nm; IDL, 23-35 nm; LDL, 18-25 nm; HDL, 5-12 nm), three-segment nanochannels 50-25-15 nm were fabricated for lipoprotein fractionation. Due to variable concentrations of surface and core lipids, lipoprotein particle sizes may vary significantly. However, I speculated that VLDL may or may not enter the channels, IDL should trap at the 25 nm barrier, LDL should trap at the 15 nm barrier and HDL would pass both barriers and accumulate at the exit.

Isolated lipoprotein fractions (VLDL, LDL, IDL, and HDL) acquired via ultracentrifugation were provided by P. Guadagno from Health Diagnostic Laboratory (Richmond, VA). The original samples were of relatively low particle number and contained high concentrations of NaBr used for density gradient ultracentrifugation. The removal of salts and the exchange of buffers were accomplished using Amicon Ultra-0.5 mL centrifugal filters (Millipore, MA) by concentrating the sample at 8,000 rpm for 4 min, then reconstituting the concentrate to the original sample volume (0.5 mL) with 200 mM pH 8.3 $NaHCO_3$ buffer. This process was repeated three times. After the third "washout," the concentrated sample was collected by spinning at 3,500 rpm for 2 min. Then, 100 μL of protein sample were labeled with 5 μL of AF 488 dissolved in DMSO overnight and exchanged into 100 mM pH 8.23 Tris buffer (containing 1 mM SDS and 0.13 w% Triton X-100 to reduce unwanted protein-surface

interactions) using the same procedures above (final protein concentrations: 9.53 mg/mL HDL, 1.38 mg/mL LDL, 2.56 mg/mL IDL).

The protein samples were diluted to a final concentration of 1 mg/mL and introduced into the channels by capillary action. It was observed that HDL with a diameter of 5–12 nm passed both height barriers and only stopped at the channel exits. LDL with a diameter of 18–25 nm accumulated at the 50 nm interfaces and channel exits. And IDL with a diameter of 23–35 nm accumulated at the 50 nm and 25 nm interfaces, with some passing through to the channel ends (**Fig. 3.5**).

Preliminary experiments showed encouraging results in that the three-segment channels were able to differentiate different lipoprotein classes by trapping them differently. However, some problems must be addressed to achieve reliable separation of lipoprotein mixtures. First, distinct adsorption was seen in the tall segments of the channels for LDL and IDL. A polymer coating of PEG was used to reduce nonspecific adsorption. Unlike in the 160-30 nm two-segment channels, where a thin coating (low PEG concentration) applied on the surface was efficient in reducing non-specific protein adsorption, a similar PEG coating was ineffective in resisting protein adsorption in 50-25-15 nm channels. When higher PEG concentration was used, liquid filling of the channels appeared to be slower and air bubbles were trapped inside the channels. I attributed these phenomena to the structural differences between the two- and three-segment channels: the three-segment channels had a larger surface-to-volume ratio and smaller average channel depth. Consequently, the flow resistance was higher and the flow rate was lower inside the three-segment channels, [13] which could result in more significant protein-surface interactions. Additionally, the compositional differences between the lipoprotein classes could also contribute

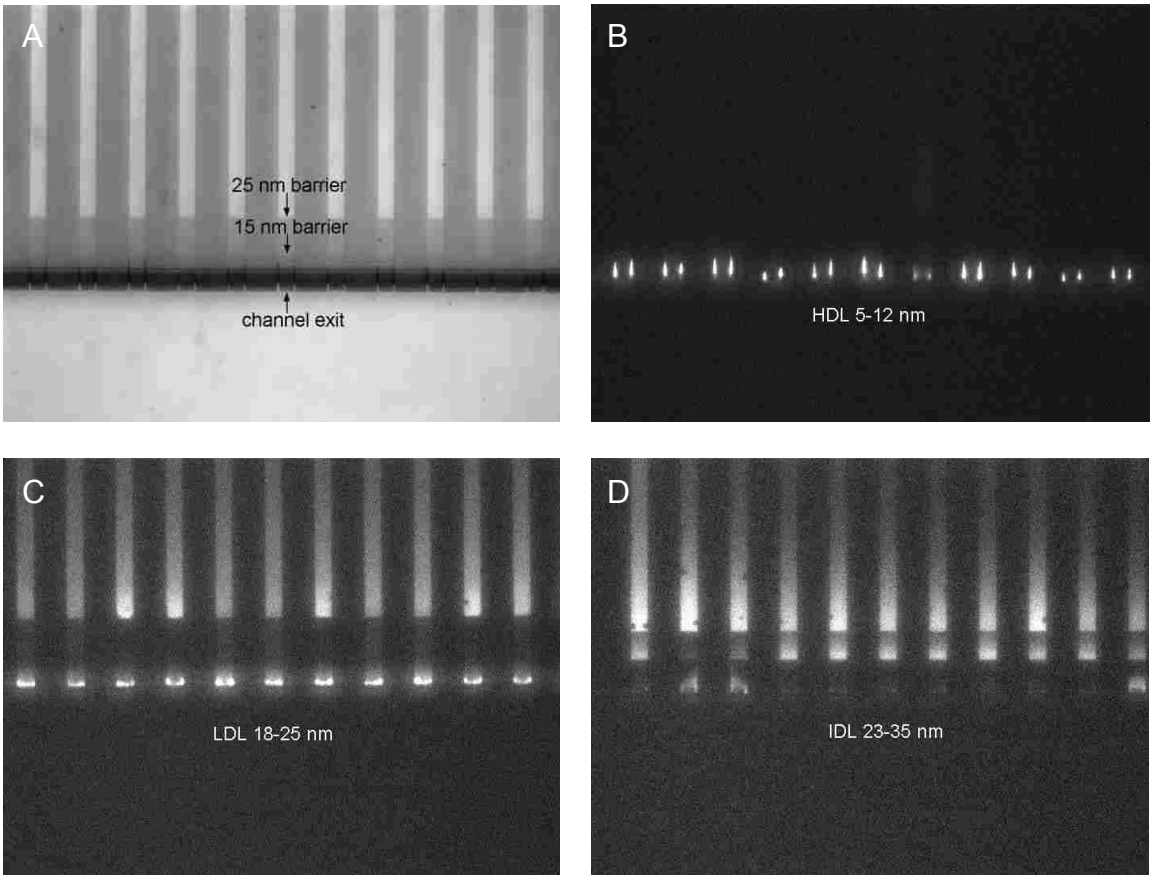

Figure 3.5 Fluorescence images showing trapping of different size lipoprotein fractions in an array of 50-25-15 nm channels. (A) Microscope view of an array of nanochannels; the lengths of three-height segments (50 nm, 25 nm and 15 nm) were 1 mm, 30 μm and 30 μm, respectively. (B) HDL with diameters between 5–12 nm passed both height barriers and only stopped at the channel exits. (C) LDL with diameters between 18–25 nm accumulated at the 50 nm interfaces and channel exits. (D) IDL with diameters between 23–35 nm accumulated at the 50 nm and 25 nm interfaces, with some stopping at the channel ends.

to non-specific adsorption. HDL has the lowest lipid content percentage compared to LDL and IDL and showed little to no adsorption (**Fig. 3.5B)**. If the assumption is correct that the surface components of lipoproteins affect how they interact with the channel surface, this would indicate that lipoproteins interact with the channel surface via free cholesterol functionalities on their surface. Second, it is possible that the existence of an entropic energy barrier at the interfaces resulted in LDL and IDL being trapped at the 50 nm interfaces even though they are both smaller than 50 nm. I tried to apply the same AC electrophoretic agitation method to proteins. Unfortunately, this resulted in worse nonspecific adsorption, which made it difficult to determine the effects of an external force on lipoprotein trapping.

Since some particles migrated to the channel exits in the LDL experiments, another possibility is that the sample contained other proteins. To verify this speculation, the LDL fraction was analyzed using sodium dodecyl polyacrylamide gradient gel electrophoresis (SDS-PAGE) in a 14% separating gel and stained with Coomassie stain. Three protein bands were obtained (**Fig. 3.6**). Calibration using molecular weight (MW) standards indicated that their corresponding MWs were approximately 250, 70 and 25 kDa, respectively.

Lipoproteins are complex aggregates of lipids and proteins held together by noncovalent forces. Each lipoprotein class has its own characteristic apolipoproteins (**Table 3.2**). For instance, ApoA1 is the major protein of HDL, and ApoB (two isoforms ApoB48 and ApoB100) is the primary protein of LDL.[14] The protein samples were incubated with 10% SDS buffer and heated at 100 ˚C for 5 to 10 min before separation, which led to apolipoprotein dissociation.[15,16] As a result, it is the isolated apolipoproteins that were most likely fractionated in SDS-PAGE. The three proteins were probably Apo B48 (chylomicron apolipoproteins) of 241 kDa or Lp(a) (LDL apolipoproteins) of 300 kDa, human serum albumin of 67 kDa (HSA is the most abundant

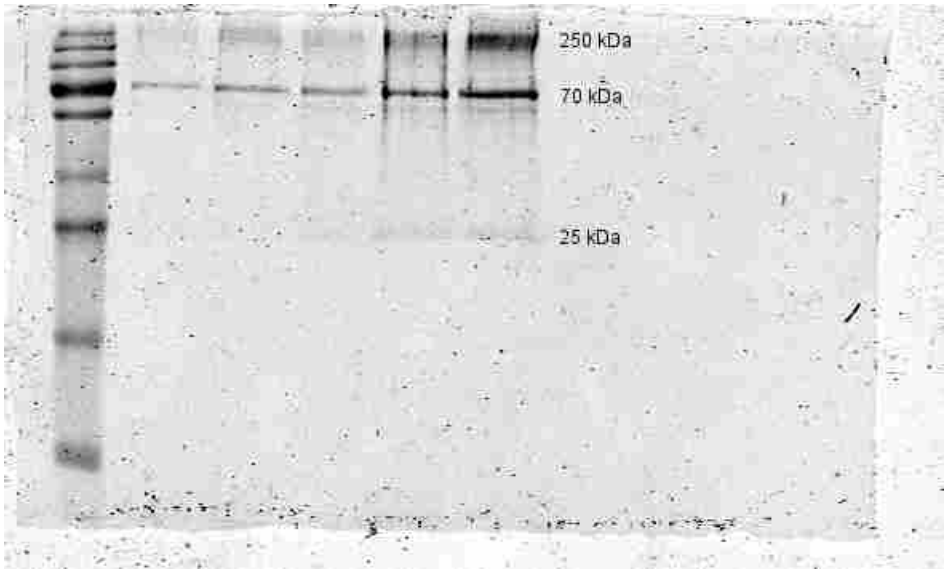

Figure 3.6 14% Tris-glycine SDS-PAGE of LDL. (Left to right) lane 1, MW standards (top to bottom: 250, 130, 100, 70, 55, 35, 25, 15 and 10 kDa); lane 2-6, a dilution series of LDL containing 1, 2.5, 5, 7.5 and 12.5 μL of 1.38 LDL, respectively.

Table 3.2 Properties of blood plasma apolipoproteins (cited from lipidlibrary.aocs.org: Plasma Lipoproteins: Composition, Structure and Biochemistry by W. W. Christie).

Table 3. The main properties of the apoproteins.*

Apoprotein	Molecular weight	Lipoprotein	Function
Apo A1	28,100	HDL	Lecithin:cholesterol acyltransferase (LCAT) activation. Main structural protein.
Apo A2	17,400	HDL	Enhances hepatic lipase activity
Apo A4	46,000	CM	
Apo AV(5)	39,000	HDL	Enhances triacylglycerol uptake
Apo B48	241,000	CM	Derived from Apo B100 – lacks the LDL receptor
Apo B100	512,000	LDL, VLDL	Binds to LDL receptor
Apo C1	7,600	VLDL, CM	Activates LCAT
Apo C2	8,900	VLDL, CM	Activates lipoprotein lipase
Apo C3	8,700	VLDL, CM	Inhibits lipoprotein lipase
Apo D	33,000	HDL	Associated with LCAT, progesterone binding
Apo E	34,000	HDL	At least 3 forms. Binds to LDL receptor
Apo(a)	300,000-800,000	LDL, Lp(a)	Linked by disulfide bond to apo B100 and similar to plasminogen
Apo H, J, L			Poorly defined functions
Apo M		HDL	Transports sphingosine-1-phosphate

* Roman numerals are sometimes used to designate apoproteins (e.g. Apo AI, AII, AIII, etc)

protein in human blood plasma) and Apo A1 (HDL apolipoproteins) of 28 kDa. Although it was not clear how much of each contaminant protein was present and how much this would affect trapping, the SDS-PAGE results did suggest that the LDL fraction obtained by GGE was not pure.

In summary, in order to separate lipoproteins using nanochannels, the surface must be passivated and the critical channel step heights must be determined. It is envisioned that fractionation of subclasses may occur with appropriately selected barrier heights. I demonstrated in Chapter 2 the potential of using multi-color fluorescence detection, which could possibly be applied to lipoprotein analysis. An external electric field may be necessary to provide flow and to help protein particles overcome energy barriers at the interfaces. Detailed size profiling requires the use of nanochannels with multiple height barriers, which poses challenges for nanofabrication.

3.8.2 Problems with bubble formation in channel filling

Successful application of nanofluidic systems demands a thorough fundamental understanding of liquid dynamics in nanoconfinements. Experimental results are presented here, demonstrating how bubbles can be eliminated by adjusting the channel dimension.

Initially, it was possible to only fabricate channel heights taller than 20 nm due to the fact that in the fabrication process, the developer AZ 300 MIF could etch away up to 20 nm of Al, which changed the channel heights and even made the short segments disappear altogether. During this time, I used taller channels, e.g., 200-50-25 nm channels, for lipoprotein analysis and observed that LDL and IDL showed similar trapping behavior, and thus could not be differentiated. When using chromium as a protective layer on the surface of Al, I was able to fabricate 100-25-15 nm channels. This modification in the fabrication process made protein

trapping feasible. However, during the filling of the 200-25-15 nm channels, solution tended to fill faster along the channel side walls, and air bubbles formed by enclosure of air in the center of the channel, which did not disappear in a period of over 10 min. Not only did the formation of bubbles increase the fluidic resistance and reduce the filling speed,[17] it also inevitably interfered with particle trapping. Therefore, this issue must be addressed in order to achieve successful trapping and separation.

Bubble formation during capillary filling of nanoconfinements with polar solvents, such as deionized water, has frequently been reported.[18-20] However, most channels reported were of a single height throughout their lengths.

The filling kinetics in nanochannels are determined by the geometry of the channel, the liquid and the surface properties. As bubble problems only arose in three-segment channels containing height barriers below 20 nm, I deduced that adding more height barriers and reducing the nanoslit cross-sectional area increased the fluidic resistance, which led to bubble formation. It was mentioned earlier that the flow resistance is inversely proportional to the channel depth and length. In order to eliminate bubble formation, I started by reducing the channel length instead of height to avoid clogging. I first tried shortening the lengths of the second and third segments from 200 μm to 100 μm, 50 μm or 30 μm, while maintaining the heights of all three segments constant. During trapping experiments, the lengths of the trapped particle bands sometimes reached tens of microns. Also, in the fabrication process, the BOE buffer etched and opened up the sidewalls of the shortest segments, making them shorter than 30 μm and even destroying the channel structures. Nevertheless, bubbles still appeared in the channels during filling. Consequently, attention focused on the abrupt height change from 200 nm down to 25 nm. Although bubbles were observed in single-height nanochannels as shallow as 27 nm, they all

quickly dissolved away.[19] Considering the fact that the trapped air bubble in the 200-25-15 nm channel arrays did not disappear in more than 10 min, it was surmised that the barrier structures prevented air from being dissolved into the solvent. In order to maintain the channel structures and solve the bubble formation problem, the heights of the first segments were decreased from 200 nm to 50 nm. With the 25 nm and 15 nm segments being 30 μm long, these new 50-25-15 nm channel arrays displayed no air bubble trapping during filling.

3.9 References

1. Yamada, M.; Seki, M. *Lab. Chip*. **2005**, *5*, 1233-1239.
2. Hamblin, M. N.; Xuan, J.; Maynes, D.; Tolley, H. D.; Belnap, D. M.; Woolley, A. T.; Lee, M. L.; Hawkins, A. R. *Lab Chip* **2010**, *10*, 173-178.
3. Batchelor, G. K. *An Introduction to Fluid Dynamics*; Cambridge University Press: Cambridge, England, 1967.
4. Mery, E.; Ricoul, F.; Sarrut, N.; Constantin, O.; Delapierre, G.; Garin, J.; Vinet, F. *Sens. Actuators, B* **2008**, *134*, 438-446.
5. Lucas, L. J.; Han, J. H.; Yoon, J. Y. *Colloids Surf., B* **2006**, *49*, 106-111.
6. Van Os, N. M.; Haak, J. R.; Rupert, L. A. *Physico-Chemical Properties of Selected Anionic, Cationic and Nonionic Surfactants*; Elsevier: Amsterdam, 1993.
7. Li, D. *Electrokinetics in Microfluidics*; Elsevier Academic Press: Amsterdam, 2004.
8. Streek, M.; Schmid, F.; Duong, T. T.; Ros, A. *Biotechnol. J.* **2004**, *112*, 79-89.
9. Pecht, M.; Radojcic, R.; Rao, G. Time Dependent Dielectric Breakdown. In *Guidebook for Managing Silicon Chip Reliability*; CRC Press: Florida, 1999; pp 26.
10. Kirby, B. J.; Hasselbrink, E.F. *Electrophoresis* **2004**, *25*, 203-213.

11. Minor, M.; vanderLinde, A. J.; vanLeeuwen, H. P.; Lyklema, J. *J. Colloid Interface Sci.* **1997**, *189*, 370.-375

12. Han, J.; Craighead, H. G. *Science* **2000**, *288*, 1026-1029.

13. Kuo, J. N.; Lin, Y. K. *Jpn. J. Appl. Phys.* **2012**, *5*, 105201(5).

14. Rader, D. J.; Hobbs, H. H. Disorder of Lipoprotein Metabolism. In *Harrison's Principles of Internal Medicine*; Fauci, A. S., Kasper, D. L., Longo, D. L., Braunwald, E., Hauser, S. L., Jameson, J. L., Loscalzo, J., Ed,; McGraw-Hill: New York, 2008; pp 334.

15. Jayaraman, S.; Cavigiolio, G.; Gursky, O. *Biochem. J.* **2012**, *442*, 703-712.

16. Jayaraman, S. Gantz, D. L.; Gursky, O. *Biochemistry* **2006**, *45*, 4620-4628.

17. Thamdrup, L. H.; Persson, F.; Bruus, H.; Kristensen, A. *Appl. Phys. Lett.* **2007**, *91*, 163505(3).

18. Eijkel, J.; Bomer, J.; Tas, N.; van den Berg, A. *Lab Chip* **2004**, *4*, 161-163.

19. Han, A.; Mondin, G.; Hegelbach, N. G.; de Rooij, N. F.; Staufer, U. *J. Colloid Inter. Sci.* **2006**, *293*, 151-157.

20. Rossi, M. P.; Ye, H.; Gogotsi, Y.; Babu, S.; Ndungu, P.; Bradley, J. *Nano Lett.* **2004**, *4*, 989-993.

Chapter 4. Nanochannels with monotonically increasing heights

4.1 Introduction

Cui and Lawes developed the first process using photoresist as sacrificial layer to fabricate micromechanical components and systems.[1] Since then, various microstructures have been created using this method.[2,3] The photoresist layer is low-cost, easy to coat and can be patterned directly. In contrast, metallic sacrificial layers require costly and time-consuming deposition processes and additional photolithography steps. This work describes a set of nanofluidic devices fabricated with photoresist as sacrificial core. Each device contains an array of 200 parallel channels consisting of two heights. The short segments monotonically increase from 30 nm to 250 nm in height from the left to right and the tall segments are 200 nm taller than the short segments.

4.2 Fabrication of wedge masks and tapered channels

We used a customized mask for fabricating tapered structures. **Fig. 4.1A** shows a taper mask created by cutting wedges out of poly(methyl methacrylate) (PMMA) using a laser cutter. The PMMA was cut in a saw-tooth pattern (7 teeth along 7 parallel line patterns). Each tooth (or taper) was approximately 10 mm long to cover the entire length of each chip. A plastic base was cut to snugly fit each of the PMMA saw tooth sections. Due to the absorption properties of PMMA, light passes through with a fairly linear power variation. Therefore, the amount of UV light transmitted onto the photoresist is dependent on the local thickness of the wedge, which subsequently results in the photoresist being spatially exposed differently and, when developed, forms a tapered structure (**Fig. 4.1B**). Light blue PMMA was found to work best at creating the

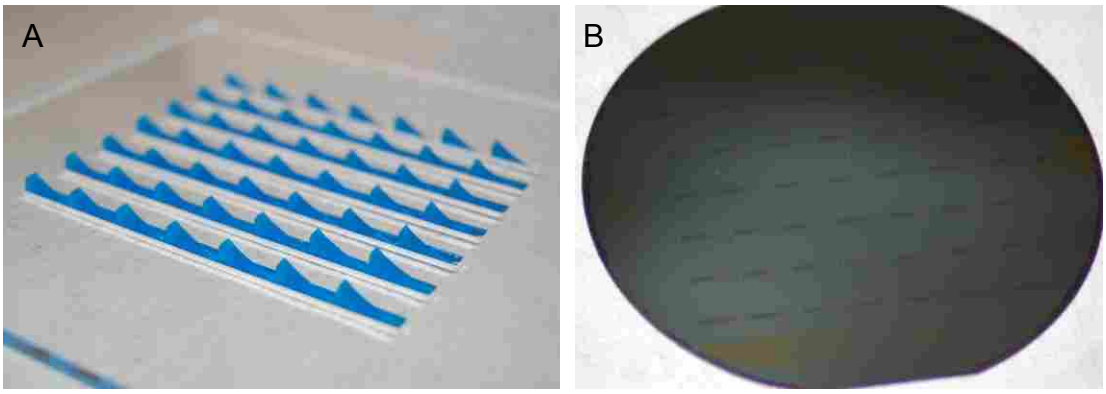

Figure 4.1 (A) Photograph of a wedge mask used to create tapered nanochannels. (B) Photograph of a wafer containing 49 silicon dies patterned with photoresist core lines; light interference is produced due to the variation in the thickness of the thin photoresist layer, indicating the presence of tapered structures.

desired taper depths. The 30–250 nm tapers were created with a wedge of 6.533 mm thickness at the tallest end.

The fabrication process for tapered channels (**Fig. 4.2**) begins with growing approximately 200 nm of PECVD silicon dioxide on top of a 4-inch silicon wafer, which forms the wettable bottom of the nanochannels. The wafer is then primed with hexamethyldisilazane (HMDS) before a 6:4 mixture of AZ 3312 and propylene glycol monomethyl ether acetate (PGMEA) is spun-on and patterned using a wedge mask to define the tapered line structures. A diluted AZ 300 MIF developer (6:7 developer/water) is used for developing the photoresist. It is ideal to reach the desired taper heights (30–250 nm in this case) directly during development. However, once the photoresist layer thickness drops below a certain level (typically 100 nm), the remaining photoresist comes off very irregularly. To overcome this problem, the low end of the taper is developed to about 100 nm, which is achieved by adjusting the development time. This parameter varied from wafer to wafer; however, for the 30–250 nm taper, it was approximately 1 min. After the channel heights are reduced to their desired values via dry etching and measured using a profilometer (**Fig. 4.3**), a second layer of AZ 3312 and PGMEA mixture is spun-on and patterned to define steps in the lines, followed by development in the diluted AZ 300 MIF developer mentioned above. Wafers are heated to at 250 ˚C and baked for 5 min before a capping layer of approximately 5 μm PECVD oxide is deposited over the core lines. Then, photoresist AZ 3330 is spun-on and pattered, exposing only the reservoir areas at the ends of the core lines. The exposed oxide is etched using buffered oxide etchant (BOE) and the masking photoresist is dissolved in acetone. The exposed photoresist lines are then etched using Piranha (3:1 mixture of concentrated sulfuric acid and hydrogen peroxide) heated to 90 ˚C. When the etching process is complete, hollow channels consisting of two heights are created. The wafer is soaked in D.I.

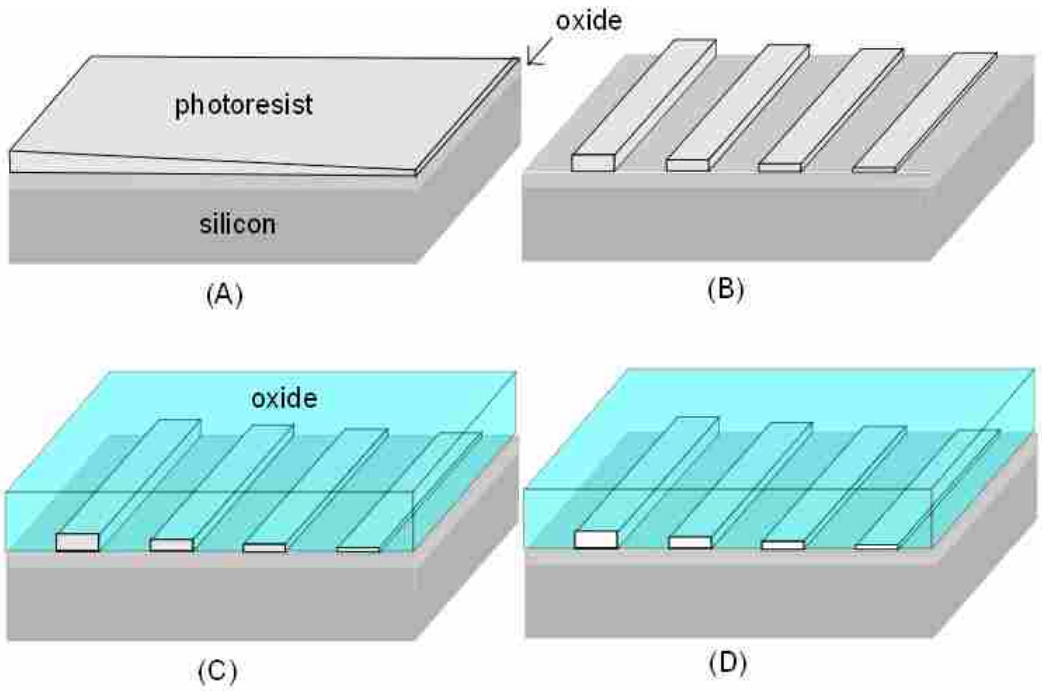

Figure 4.2 Drawings illustrating the fabrication process involved in making tapered nanochannels.

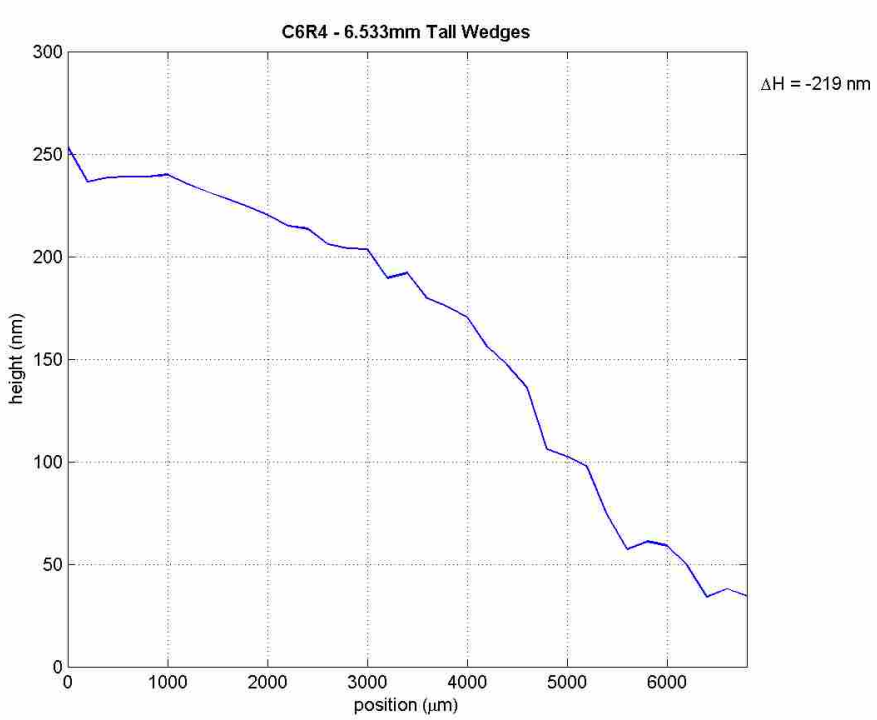

Figure 4.3 Profilometry analysis of photoresist-formed nanochannel core lines tapered from approximately 30 nm to 250 nm.

water overnight before use.

4.3 Trapping of polymer beads

The tapered channels were used for trapping fluorescently labeled 30 nm polyacrylonitrile polymer beads suspended in 100 mM pH 8.3 Tris-HCl buffer containing 1 mM SDS and 0.13% Triton X-100 to prevent adsorption and aggregation. The concentrations of both beads were 6×10^{12} particles/mL. The 30 nm particles were tested in an array of 30–250 nm channels. Clear differential trapping behavior was observed in a 22-channel section, in which the barriers tapered from 30 nm to 53.1 nm (**Fig. 4.4A**). The barrier height was calculated based on the profiled average height of the taper array (30–250 nm) and the average height difference between every two adjacent channels (1.1 nm), assuming the height increased (or decreased) linearly from one side of the chip to the other. It can be seen that the fluorescence intensity gradually decreased from left to right at the barriers (*I*), and increased at the channel ends (*E*). Using the two sets of fluorescence intensity data (*I* and *E*) allowed me to calculate the trapped/total ratios ($T/t = I/(I+E)$), which were then plotted versus channel height. This curve displays the same trend as the slit model (i.e., $T/t = d_p/h$, see section 2.3) predicts, although the values are lower (**Fig. 4.4B**). As mentioned before, since the slit model is derived from Giddings' model, which defines diffusion as the sole driving force for separation, it is expected that the experimental T/t should be lower in our case because the existence of capillary force provides an external force to help the particles overcome the energy barrier when they are introduced into the channels. Thus, fewer particles should be trapped at the channel interface.

Trapping of 30 nm particles was also tested in the other sections of the same chip. Unfortunately, they did not show a clear difference in terms of trapping. This can be attributed to the discrepancy between the profiled depths of the photoresist core lines prior to oxide capping

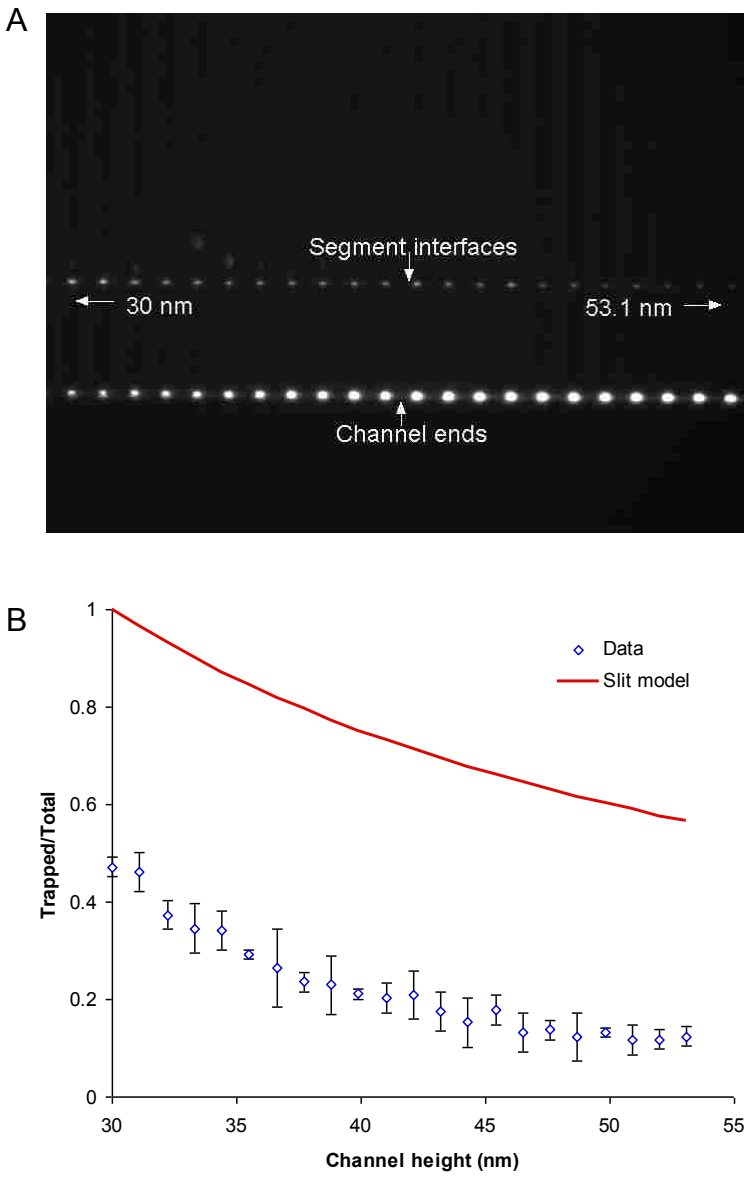

Figure 4.4 (A) Image showing trapping of 30 nm fluorescently labeled PAN beads in an array of channels with an interface tapering from 30 nm to 53.1 nm (left to right). The particles clearly display differential trapping behavior. (B) Data analysis of trapped/total particles versus channel height, showing the same trend predicted by the slit model. Error bars represent the standard deviation of three measurements.

layer deposition and the actual channel heights after photoresist was dissolved by hot piranha. It is a common practice when using piranha solution to clean the photoresist residue from the silicon wafers. However, it was reported that using piranha solution to dissolve photoresist tended to clog the channels.[4] It is likely that the etching process leaves a residue, which forms a thin film on the inner channel surface and changes its depth and width, especially considering that etched materials can only slowly diffuse out of the channels. Soaking with water may be insufficient to remove the residue. It has been demonstrated that an oxygen plasma is more efficient than piranha for removing photoresist,[4] although it would be difficult to carry out in enclosed nanochannels such as those described here.

In this study, a total of eight sets of tapered nanochannels of different dimensions were fabricated and tested. Fewer than a dozen devices from two wafers (each containing 49 dies) showed differential trapping of 30 nm particles in a section of the channels on the chip. The experimental data followed the trend predicted by the slit model, although there was a discrepancy of 50% between them. These results indicated that it was possible to fabricate tapered nanochannels using photoresist as sacrificial core, and then use them for differential trapping, although the repeatability was still low. The fabrication of tapered channels should be further developed to improve channel height precision and linearity in channel height change across the channel arrays. Ideally, the nanofluidic chip should display differential trapping behavior across the entire array of 200 channels. The ultimate goal is to use the tapered channels for separating mixtures and determining their size distributions based on barrier heights and trapped/total data. Additional channel dimensions and more particle sizes must be investigated to adjust the slit model.

4.4 References

1. Cui, Z.; Lawes, R. A. *J. Micromech. Microeng.* **1997**, *1*, 128-130.

2. Peeni, B. A.; Lee, M. L.; Hawkins, A. R.; Woolley, A. T. *Electrophoresis* **2006**, *27*, 4888-4895.

3. Subramani, B. G.; Selvaganapathy, P. R. J. *Micromech. Microeng.* **2009**, *19*, 015013(10).

4. Mao, P.; Wang, H-T.; Yang, P.; Wang, D. *Anal. Chem.* **2011**, *83*, 6082-6089.

Chapter 5. Conclusions and future work

Reports of novel micro/nanostructures designed to separate biomacromolecules and bioparticles are increasing in number, and these studies have greatly advanced our understanding of nanoscale fluidics and nanoparticle behavior in confined channels. In the work described in this dissertation, I developed a simple, fast nanosieving method and demonstrated its applications for size-based separation of engineered and biological nanoparticles. Specifically, three types of nanochannels were fabricated, including two-segment nanochannels (channels with two different channel height segments), three-segment nanochannels (channels with three different channel height segments), and tapered nanochannels (channels with monotonically changing barrier heights from one side of the nanofluidic chip to the other). I demonstrated the successful trapping of polymer nanobeads and two types of virus capsids (30 nm HBV and 120 nm HSV-1) using two-segment nanochannels. Furthermore, I studied the fractionation of nanoparticles in three-segment nanochannels. The effects of adding surfactants and applying an alternating current electric field on particle distribution were investigated, both of which aided in the prevention of channel clogging. Most recently, I applied the nanosieving method to lipoprotein analysis. Promising results were obtained, indicating that it should eventually be possible to fractionate the major lipoprotein classes (IDL, LDL and HDL) using three-segment nanochannels. I studied the protein-resistant performance of polyethylene glycol (PEG) coatings and used dual-color fluorescence detection for the separation of a binary protein mixture. Finally, I successfully fabricated tapered channels using photoresist sacrificial materials and applied them to trapping 30 nm polymer nanobeads.

These results demonstrate the potential of using nanosieves for separating proteins. However, three challenging issues remain: nonspecific adsorption, clogging (or aggregation) and

an energy barrier at the channel interfaces. In order to achieve the ultimate goal of fractionating lipoprotein mixtures, the inner channel surface must be passivated via dynamic modification to minimize protein-wall interactions. More trapping tests must be performed to determine the critical step heights, at which each lipoprotein class would stop or pass. It is envisioned that fractionation of subclasses may occur with barrier heights in between. I showed the possibility of doing multi-color fluorescence detection, which could potentially be applied to lipoprotein analysis. An external electric field may be necessary to propel flow and help protein particles overcome the energy barrier at the interfaces. Detailed size profiling requires the use of nanochannels with multiple height barriers, which poses challenges for nanofabrication. Also, meticulous characterization of flow dynamics inside these channels is required.

With tapered nanochannels, the experimental data generally followed trends predicted by the slit model, although there was a discrepancy of 50% between them. More channel dimensions and particle sizes should be investigated to determine how the original slit model can be adjusted to address our channel structures better and predict trapping more accurately. More studies should also be done to determine the reasons behind the differences in trapping behavior for rigid and flexible particles, and between lipoproteins and other types of proteins. The fabrication of tapered channels should be further developed in order to improve channel height precision. Ideally, differential trapping behavior across the entire array of 200 channels should be possible. I hope that the tapered channels can eventually be used for separating nanoparticle mixtures and analyzing their size distributions based on barrier heights and trapped/total data.

In summary, micro/nanofabricated structures have opened new possibilities for efficient separation of biomolecules. Advances in fabrication techniques enable researchers to control geometrical designs and provide insight into separation mechanisms at the molecular level.

Multi-dimensional or anisotropic structures hold great future promise for high resolution, high throughput separations. Although many challenges continue to plague research efforts, such as nonspecific adsorption, clogging and detection of extremely low-concentration analytes, there is no doubt that nanotechnologies will continue to grow at a rapid pace, since they offer unique opportunities that are not addressed by any of the conventional methods.